Doctoral Thesis

Topology Conversion and Mesopore Generation in Metal-Organic Frameworks

Seok Jeong

Department of Chemistry

Graduate School of UNIST

2019

Topology Conversion and Mesopore Generation in Metal-Organic Frameworks

Seok Jeong

Department of Chemistry

Graduate School of UNIST

Topology Conversion and Mesopore Generation in Metal-Organic Frameworks

A thesis/dissertation
submitted to the Graduate School of UNIST
in partial fulfillment of the
requirements for the degree of
Doctor of Philosophy

Seok Jeong

06/ 07/ 2019
Approved by

_____

Advisor
Myoung-soo Lah

Topology Conversion and Mesopore Generation in Metal-Organic Frameworks

Seok Jeong

This certifies that the thesis/dissertation of Seok Jeong is approved.

06/ 07/ 2019

Signature

_____

Advisor: Myoung soo Lah

Signature

_____

Hoi ri Moon

Signature

_____

Min Kim

Signature

_____

Jong-Beom Baek

Signature

_____

Nak Cheon Jeong

Abstract

Part 1

Non-interpenetrated three-dimensional (3D) metal−organic frameworks (MOFs) with both an interpenetration-favorable(3,5)-c **hms** topology and an interpenetration-unfavorable (3,5)-c **gra** topology are converted to doubly interpenetrated analogues with **hms-c** topology by thermal treatment, even in the absence of solvent. Depending on the conversion temperature and the properties of the pillaring ligand in the non-interpenetrated 3D MOF, which is based on two-dimensional sheets with 3-c **hcb** topology pillared by neutral ditopic linkers, the pillaring ligands in the interpenetrated MOFs produced are partially removed during the thermal conversions, leading to interpenetrated MOFs that simultaneously contain both micro- and mesopores.

Part 2

As opposed to the growth mechanisms of metal-organic frameworks (MOFs) known to date, **[Ni(HBTC)(bipy)]** is thought to follow an crystallization by particle attachment (CPA), which means, a large number of domains are attached to form single crystal. On the other hand, non-interpenetrated **[Ni(HBTC)(bipy)]** is converted to doubly interpenetrated **[Ni(HBTC)(bipy)]** through thermal treatment. We report the mechanism of a new mesopore generation that has not been encountered so far, combining these two characteristics. It can also control the size of mesopores according to thermal treatment conditions.

Contents

1. Topology Conversions of Non-Interpenetrated Metal-Organic Frameworks to Doubly Interpenetrated Metal-Organic Frameworks

Scheme 1.1 Conversion of non-interpenetrated networks with both interpenetration-favorable **hms** topology and with self-interpenetration-unfavorable **gra** topology to doubly interpenetrated networks with **hms-c** topologies.

Scheme 1.2. Proposed conversion mechanisms from both non-interpenetrated networks with **hms** topology and with **gra** topology to a doubly interpenetrated network with **hms-c** topology.

Figure 1.1 Ball-and-stick diagrams of the single crystal structure of **3** and **4**.

Figure 1.2. Comparison of the PXRD patterns of as-synthesized **3** and **4.**

Figure 1.3. N_2 sorption isotherms of **3a** and **4a** at 77 K.

Figure 1.4. BET surface area calculation of **3a**.

Figure 1.5. BET surface area calculation of **4a**.

Figure 1.6. Pore size distributions of **3a** and **4a**.

Figure 1.7. Temperature-dependent PXRD patterns of **1** and **2**

Figure 1.8. Temperature dependent PXRD patterns of **3** and **4**.

Figure 1.9. Single crystal structure of **5** with **hms-c** topology.

Figure 1.10. Ball-and-stick drawing and a space-filling drawing of an cage in **5**.

Figure 1.11. Single crystal structure of **6** showing a 3D network of **hms-c** topology.

Figure 1.12. Ball-and-stick drawing and space-filling drawing of a cage in **6**.

2. New Mechanism of Mesopore Generation in Metal-Organic Frameworks

Figure 2.2. Optical photographs of **1** and **1(300, 1)**.

Figure 2.3. SEM images of **1. 1(200, 1), 1(250, 1), 1(275, 1), 1(300, 1)** and **1(350, 1)** top view.

Figure 2.4. SEM images of **1, 1(200, 1), 1(250, 1), 1(275, 1), 1(300, 1)** and **1(350, 1)** side view.

Figure 2.5. SEM images of grinded (a) **1** (b) **1(200, 1)** (c) **1(300, 1)** (d) **1(350, 1)**

Figure 2.6. The PXRD patterns of **1(200,t)** and **1(250,t)**.

Figure 2.7. The PXRD patterns of **1(275,t)** and **1(300,t)**.

Figure 2.8. The PXRD patterns of **1(350,1)** and **1(350,2)**.

Figure 2.9. The N_2 sorption isotherms of **1(T, 1)** at 77 K and the pore size distributions, and The pore size distributions of **1(T, t)** depending on aging time and temperature.

Figure 2.10. The N_2 sorption isotherms of (a) **1(200, t)** at 77 K. Adsorption and desorption isotherms are represented by filled and empty circles, respectively. (b) The pore size distributions and cumulative in the box of **1(200, t)**

Figure 2.11. The N_2 sorption isotherms of (a) **1(250, t)** at 77 K. Adsorption and desorption isotherms are represented by filled and empty circles, respectively. (b) The pore size distributions and cumulative in the box of **1(250, t)**

Figure 2.12. The N_2 sorption isotherms of (a) **1(275, t)** at 77 K. Adsorption and desorption isotherms are represented by filled and empty circles, respectively. (b) The pore size distributions and cumulative in the box of **1(275, t)**

Figure 2.13. The N_2 sorption isotherms of (a) **1(300, t)** at 77 K. Adsorption and desorption isotherms are represented by filled and empty circles, respectively. (b) The pore size distributions and cumulative in the box of **1(300, t)**

List of tables

Table 2.2. Pore properties of **1** and **1(T,t)**

I. Topology Conversions of Non-Interpenetrated Metal-Organic Frameworks to Doubly Interpenetrated Metal-Organic Frameworks

1.1 Introduction

Metal-organic frameworks (MOFs) are interesting microporous materials that are composed of metal ions and/or metal clusters that act as multitopic inorganic nodes with organic ligands acting as linkers.[1-4] It is important to control the degree of interpenetration in MOFs because this affects not only their porosity but also their stability. MOFs thermodynamically prefer a densely packed interpenetrated structure when the net topology and dimensions of the building blocks allow for it.[5-8] It is well known that MOFs of interpenetration-favorable self-dual topologies such as dia and pcu show strong tendencies for interpenetration.[9-11] When the net topologies of a MOF does not allow interpenetration because of collision between the networks,[12] a non-interpenetrated MOF can be prepared that can have an extremely large porosity.[13-18] Interpenetration can be controlled, even for the MOFs with interpenetration-favorable topologies, either through ligand design[19,20] or by controlling synthetic conditions such as reactant concentration, temperature, counter ions, and the use of different solvents or templating agents.[21-24]

The degree of interpenetration of MOFs can also be controlled by post-synthetic modification. Non-interpenetrated MOFs with an interpenetration-favorable topology can be transformed into their more densely packed interpenetrated analogues. For instance, the non-interpenetrated MOF-123, which has pcu topology, was transformed into the doubly interpenetrated MOF-246, which possesses pcu-c topology, by removing its coordinated solvent molecules.[25] Similar transformations from non- to twofold interpenetrated MOFs have been reported for two other systems: [Cd(tp)(bipy)] (H2tp = terephthalic acid; bipy = 4,4′-bipyridine) and [Cd(atp)(bipy)] (H_2atp = 2-aminoterephthalic acid).[26] Heating the doubly interpenetrated MOF [Zn2(ndc)2(bipy)] (H_2ndc = naphthalene dicarboxylic acid) with pcu-c topology resulted in a triply interpenetrated analogue with pcu-c3 topology in a single-crystal-to-single-crystal (SCSC) fashion.[27] A conversion from the 5-fold interpenetrated MOF $[Ag_6Cl(atz)_4](OH)$ (atz = 3-amino-1,2,4-triazolate) to a 6-fold interpenetrated analogue has even been observed.[28]

A network with a hms topology, which is a (3,5)-c 3D network with ditopic pillars between 2D sheets with 3-c hcb topologies stacked in an eclipsed fashion via alternating 3-c nodes, is favorable for

interpenetration because hms is self-dual.[9] However, a network with gra topology, which is another (3,5)-c 3D network with ditopic pillars between 2D sheets stacked in staggered fashion via alternating 3-c nodes, is less favorable for self-interpenetration than the isomeric network with hms topology because gra is not self-dual.[29] Self-interpenetrated networks with gra-c (catenated gra) topologies will face the more steric repulsions between the interpenetrated networks than isomeric networks with hms-c topology. When the organic linkers of a MOF with gra topology are long enough, the steric repulsion between the interpenetrated networks can be released, allowing a triply interpenetrated MOF with gra-c3 topology to form.[30]

Here, we report the preparation of non-interpenetrated 3D MOFs with not only (3,5)-c hms topologies but also with (3,5)-c gra topologies, where the non-interpenetrated MOFs are based on 2D sheets with 3-c hcb topologies pillared by two different neutral ditopic linkers. The less densely packed non-interpenetrated MOFs with both the interpenetration-favorable hms topology and the self-interpenetration-unfavorable gra topology can be thermally converted to generate more densely packed twofold interpenetrated MOFs with hms-c topologies even in the absence of solvent (Scheme 1). However, conversion to a twofold interpenetrated MOF with gra-c topology was not observed regardless of the net topologies of the non-interpenetrated MOFs because of severe repulsion or collision between interpenetrated networks.

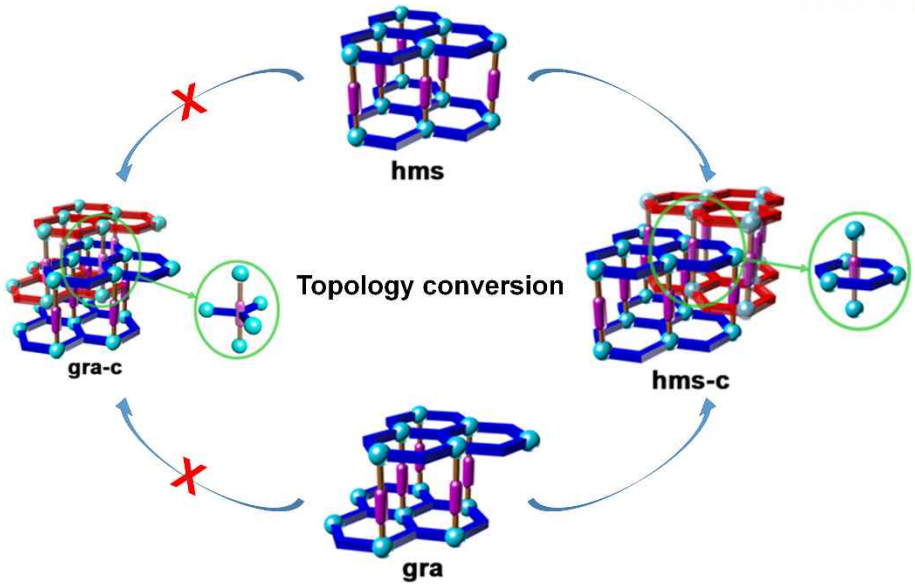

Scheme 1.1 Conversion of non-interpenetrated networks with both interpenetration-favorable **hms** topology and with self-interpenetration-unfavorable **gra** topology to doubly interpenetrated networks with **hms-c** topologies.

1.2 EXPERIMENTAL SECTION

General Procedures

All reagents were purchased from commercial sources and used without further purification. Elemental analyses were conducted using a Flash 2000 elemental analyzer at the Ulsan National Institute of Science and Technology, Korea. Fourier transform–infrared (FT–IR) spectra were recorded from KBr pellets using a NICOLET iS 10 FT–IR spectrophotometer (4000–400 cm^{-1}). ^1H nuclear magnetic resonance (NMR) spectra were recorded using a VNMRS 600 MHz FT-NMR spectrophotometer. Powder X-ray diffraction (PXRD) data were recorded using a Bruker D2 Phaser automated diffractometer at room temperature with a step size of 0.02° in 2θ angle. Simulated PXRD patterns were calculated with Materials Studio software[31] using single-crystal data. All gas sorption isotherms were measured using a BELSORP-max (BEL Japan, Inc.) with a standard volumetric technique using N_2 (with purity of 99.999%) as an adsorbate.

Preparation of non-interpenetrated MOFs.

[Ni(HBTC)(bipy)]-hms (1) and [Ni(HBTC)(bipy)]-gra (2). [Ni(HBTC)(bipy)]-hms (**1**) ($HBTC^{2-}$ = singly protonated 1,3,5-benzene tricarboxylate), which has **hms** topology, and [Ni(HBTC)(bipy)]-gra (**2**), which exhibits a **gra** topology, were prepared according to previously reported procedures.[32-34] Activated **1a** and **2a** were obtained by vacuuming (~10^{-2} torr) the corresponding as-synthesized crystals presoaked in methylene chloride (MC) at ambient temperature for 1 d.

[Ni(HBTC)(azpy)]-hms (3). A mixture of $Ni(NO_3)_2 \cdot 6H_2O$ (0.029 g, 0.100 mmol), 1,3,5-benzene tricarboxylic acid (H_3BTC, 0.021 g, 0.10 mmol), and 4,4′-azopyridine (azpy, 0.037 g, 0.20 mmol) was dissolved in a mixture of *N,N*-dimethylformamide (DMF)/MeOH (10 mL, 1:1 ratio). The solution was heated at 85 °C for 1 d in a tightly sealed 20 mL vial to form red crystals of [Ni(HBTC)(azpy)]-hms (**3**) with **hms** topology. The crystals were harvested and washed with fresh DMF, and then air-dried under ambient conditions for an hour (Yield = 0.029 g (61%)). Activated **3a** was prepared by vacuuming (~10^{-2} torr) as-synthesized **3** presoaked in MC at ambient temperature for 1 d. IR (KBr, cm^{-1}): 3195 (w, b), 3099 (w, b), 1694 (w), 1660 (m), 1605 (s), 1538 (s), 1494 (w), 1434 (s), 1417 (m), 1360 (s), 1225 (m), 1100 (m), 1050 (m), 1020 (m), 932 (w), 838 (s), 757 (w), 742 (w), 714 (m), 680 (w). EA was performed using activated **3a** that had been exposed to ambient conditions for 1 d prior to analysis. EA for $Ni(HBTC)(azpy)(H_2O)_{1.5}$ ($C_{19}H_{15}N_4O_{7.5}Ni$, fw = 478.04 g/mol). Found (Calcd): C = 47.82 (47.74)%; H = 3.18 (3.16)%; N = 12.18 (11.72)%.

[Ni(HBTC)(azpy)]-gra (4). A mixture of $Ni(NO_3)_2 \cdot 6H_2O$ (0.029 g, 0.10 mmol), H_3BTC (0.021 g, 0.10 mmol), and azpy (0.037 g, 0.20 mmol) was dissolved in 10 mL DMF. The solution was heated at 85 °C for 1 d in a tightly sealed 10 mL vial to form red crystals of [Ni(HBTC)(azpy)]-gra (**4**) with **gra** topology. The crystals were harvested and washed using fresh DMF, and then air-dried under ambient conditions for 1 h (Yield = 0.028 g (57%)). Activated **4a** was prepared by vacuuming (~10^{-2} torr) as-synthesized **4** presoaked in MC at ambient temperature for 1 d. IR (KBr, cm^{-1}): 3355 (s, b), 1700 (w), 1663 (m), 1608 (s), 1558 (s), 1490 (w), 1433 (s), 1419 (s), 1366 (s), 1261 (m), 1228 (m), 1189 (w), 1102 (m), 1051 (m), 1021 (m), 933 (w), 844 (m), 761 (m), 742 (w), 717 (m). EA was performed using activated **4a** exposed to ambient conditions for 1 d prior to analysis. EA for $Ni(HBTC)(azpy)(H_2O)_{0.9}$

($C_{19}H_{16.6}N_4O_{8.3}Ni$, fw = 492.5 g/mol). Found (Calcd): C = 46.46 (46.34)%; H = 3.87 (3.40)%; N = 11.20 (11.38)%.

Preparation of doubly interpenetrated [Ni(HBTC)(bipy)]-hms-c (5). Approximately 10 mg of single crystals of as-synthesized **1** was prewashed with fresh DMF and air-dried at under ambient conditions for 3 h. The sample was then heated to 300 °C under a flow of nitrogen gas at a heating rate of 5 °C min^{-1}, aged for 30 min at 300 °C, then slowly cooled to room temperature. **5** was also obtained from single crystals of as-synthesized **2** instead of as-synthesized **1** by the same procedure described above. EA for $Ni(HBTC)(bipy)_{0.89}(H_2O)_{0.72}$ ($C_{17.9}H_{12.56}N_{1.78}O_{6.72}Ni$, fw = 418.79 g/mol). Found (Calcd): C = 51.35 (51.34)%; H = 3.19 (3.02)%; N = 5.93 (5.95)%. Activated **5a** was prepared by vacuuming (~10^{-2} torr) as-synthesized **5** at 100 °C for 3 h.

Preparation of doubly interpenetrated [Ni(HBTC)(azpy)]-hms-c (6). Approximately 10 mg of single crystals of as-synthesized **3** were prewashed with fresh DMF and air-dried under ambient conditions for 3 h. The sample was heated to 250 °C under flowing nitrogen gas at a heating rate of 5 °C min^{-1}, aged for 30 min at 250 °C, and then slowly cooled to room temperature. **6** was also obtained from single crystals of as-synthesized **4** instead of as-synthesized **3** by the same procedure described above. EA for $Ni(HBTC)(azpy)_{0.95}(H_2O)_{0.56}$ ($C_{18.5}H_{12.72}N_{3.8}O_{6.56}Ni$, fw = 451.89 g/mol). Found (Calcd): C = 49.16 (49.17)%; H = 2.84 (2.84)%; N = 11.78 (11.78)%. Activated **6a** was prepared by vacuuming (~10^{-2} torr) as-synthesized **6** at 100 °C for 3 h.

Single crystal structure analyses of the MOFs

The diffraction data of single crystals of **3** and **5** coated with Paratone oil were measured at 173 K using Mo Kα radiation with an X-ray diffraction camera system and an imaging plate equipped with a graphite crystal incident beam monochromator. The Rapid Auto software[35] was used for data collection and data processing. The diffraction data of single crystals of **4** and **6** coated with Paratone oil were measured at 173 and 100 K, respectively, with synchrotron radiation (λ = 0.70000 and 0.67000 Å, respectively) on an ADSC Quantum-210 detector at 2D SMC with a silicon (111) double crystal monochromator (DCM) at the Pohang Accelerator Laboratory, Korea. The ADSC Q210 ADX software[36] was used for data

collection (detector distance was 63 mm, omega scan; $\Delta\omega = 1°$, exposure time was 1 s per frame) and HKL3000sm (ver. 703r)[37] was used for cell refinement, reduction, and absorption correction. All the crystal structures were solved via a direct method using the XS program and refined by full-matrix least-squares calculations using the XL program of the SHELX program package.[38]

[Ni(HBTC)(azpy)]-hms, 3. A orange, plate shaped crystal, 0.30 × 0.29 × 0.10 mm^3, $C_{57}H_{36}NO_{18}Ni_3$, fw = 1353.11 $g{\cdot}mol^{-1}$, monoclinic, space group *Cm*, a = 16.384(3) Å, b = 28.376(6) Å, c = 13.079(3) Å, $\beta = 95.57(3)°$, V = 6052(2) $Å^3$, Z = 2, μ (Mo Kα, $\lambda = 0.71073$ Å) = 0.503 mm^{-1}, 18,603 reflections were collected, 8,594 were unique [$R_{int} = 0.2363$]. One and half nickel atoms (one atom was at a general position and the other nickel site of 0.5 site occupancy at a Wyckoff 2*a* site (*m* site symmetry)), one and half $HBTC^{2-}$ ligands (one $HBTC^{2-}$ ligand in a $H_{1.5}BTC^{1.5-}$ form was at a general position and the other $HBTC^{2-}$ ligand in a BTC^{3-} form of 0.5 site occupancy was at another Wyckoff 2*a* site (*m* site symmetry)), and one and half azpy ligands (one azpy ligand was at a general position and the other azpy ligand of 0.5 site occupancy was at the other Wyckoff 2*a* site (*m* site symmetry)) were observed as an asymmetric unit. All non-hydrogen atoms were refined anisotropically; the hydrogen atoms were assigned isotropic displacement coefficients U(H) = 1.2U (C), and their coordinates were allowed to ride on their respective atoms. The least-squares refinement of the structural model was performed under geometry restraints and displacement parameter restraints such as DFIX, DANG, FLAT, ISOR, and SIMU. The final refinement was performed with the modification of the structural factors for the electron densities of the disordered solvents (3819 $Å^3$ (63.1% of the total unit cell volume); 786 electrons correspond to ~ 14 DMF molecules per unit cell) using the SQUEEZE option of PLATON.[39] The carboxylic hydrogen atoms of the $H_{1.5}BTC^{1.5-}$ ligand site were not included in the least-squares refinement. Refinement of the structure converged at a final $R1 = 0.1322$ and $wR2 = 0.3130$ for 3897 reflections with $I > 2\sigma(I)$; $R1 = 0.2243$ and $wR2 = 0.3923$ for all 8954 reflections. The largest difference peak and hole were 1.221 and −0.966 $e{\cdot}Å^{-3}$, respectively.

[Ni(HBTC)(azpy)]-gra, 4. An orange, plate shaped crystal, 0.080 × 0.080 × 0.030 mm^3, $C_{57}H_{36}NO_{18}Ni_3$, fw = 1353.11 $g{\cdot}mol^{-1}$, monoclinic, space group *Pbcn*, a = 28.676(6) Å, b = 16.573(3) Å, c = 26.148(5)

Å, β = 90.02(3)°, V = 12427(4) Å^3, Z = 4, μ (Mo Kα, λ = 0.70000 Å) = 0.468 mm^{-1}, 56,027 reflections were collected, 32,259 were unique [R_{int} = 0.1502]. Three nickel atoms (two atoms were at general positions and the other two nickel sites of 0.5 site occupancy were at Wyckoff 2*a* and 2*b* sites (2 site symmetry)), three $HBTC^{2-}$ ligands (two $HBTC^{2-}$ ligands in a $H_{1.5}BTC^{1.5-}$ form were at general positions and the other two $HBTC^{2-}$ ligand sites in a BTC^{3-} form of 0.5 site occupancy were at the other Wyckoff 2*a* and 2*b* sites (2 site symmetry)), and three azpy ligands were observed as an asymmetric unit. All non-hydrogen atoms were refined anisotropically; the hydrogen atoms were assigned isotropic displacement coefficients U(H) = 1.2U (C), and their coordinates were allowed to ride on their respective atoms. The least-squares refinement of the structural model was performed under geometry restraints and displacement parameter restraints such as DFIX, DANG, FLAT, ISOR, SIMU, and DELU. The final refinement was performed with the modification of the structural factors for the electron densities of the disordered solvents (7489 Å^3 (64.5% of the total unit cell volume); 2443 electrons correspond to ~61 DMF molecules per unit cell) using the SQUEEZE option of PLATON.[S6] The carboxylic hydrogen atoms of the $H_{1.5}BTC^{1.5-}$ ligand site were not included in the least-squares refinement. Refinement of the structure converged at a final *R*1 = 0.0945 and *wR*2 = 0.2271 for 10,592 reflections with I > 2σ(I); *R*1 = 0.24149 and *wR*2 = 0.2693 for all 32,259 reflections. The largest difference peak and hole were 0.599 and –0.645 e·Å^{-3}, respectively. Though the symmetry of the final structure model under thye *C*2 space group indicated the possibility of the space group of the structure being *C*2/*c*, the refinement of the structural model under the *C*2/*c* space group converged at higher R values (*R*1 = 0.2461 and *wR*2 = 0.3139 for 5247 reflections with I > 2σ(I); *R*1 = 0.3139 and *wR*2 = 0.5684 for all 14066 reflections) than those obtained under the *C*2 space group.

[Ni(HBTC)(bipy)]-hms-c, 5. A green, plate shaped crystal, 0.45 × 0.24 × 0.11 mm^3, $C_{19}H_{12}N_2O_6Ni$, fw = 423.02 g·mol^{-1}, hexagonal, space group $P6_3/mcm$, a = b = 16.833(2) Å, c = 11.241(2) Å, V = 2758.7(10) Å^3, Z = 6, μ (Mo Kα, λ = 0.71073 Å) = 1.094 mm^{-1}, 22,841 reflections were collected, 1,175 were unique [R_{int} = 0.1152]. One nickel site of 0.25 site occupancy at a Wyckoff 6*g* site (*m*2*m* site symmetry), two $HBTC^{2-}$ ligand sites of a total of 1/3 site occupancy with $H_{1.5}BTC^{1.5-}$ form at a

Wyckoff 4*c* site (-6 site symmetry) and with BTC^{3-} form at a Wyckoff 2*a* site (-62m site symmetry), and one bipy ligand site of 0.25 site occupancy at another Wyckoff 6*g* site (*m*2*m* site symmetry) were observed as an asymmetric unit. All non-hydrogen atoms were refined anisotropically; the hydrogen atoms were assigned isotropic displacement coefficients U(H) = 1.2U (C), and their coordinates were allowed to ride on their respective atoms. The carboxylic hydrogen atom of the $H_{1.5}BTC^{1.5-}$ ligand site was not included in the least-squares refinement. Final refinement of the structure converged at a final *R*1 = 0.1244 and *wR*2 = 0.2781 for 938 reflections with I > 2σ(I); R1 = 0.1442 and *wR*2 = 0.2876 for all 1175 reflections. The largest difference peak and hole were 1.745 and −1.833 e·Å^{-3}, respectively.

[Ni(HBTC)(azpy)]-hms-c, 6. A red brown, plate shaped crystal, 0.040 × 0.040 × 0.008 mm^3, $C_{19}H_{12}N_4O_6Ni$, fw = 451.04 g·mol^{-1}, trigonal, space group *P*-3, a = b = 16.657(2) Å, c = 13.173(3) Å, V = 3165.4(11) Å^3, Z = 6, μ (synchrotron, λ = 0.6700 Å) = 0.816 mm^{-1}, 21,617 reflections were collected, 3,954 were unique [R_{int} = 0.1127]. One nickel atom at a general position, three $HBTC^{2-}$ ligand sites of a total of one site occupancy with $H_{1.5}BTC^{1.5-}$ form at a Wyckoff 2*c* site (3 site symmetry) and with BTC^{3-} form at a Wyckoff 2*a* site (-62m site symmetry), and one statistically disordered azpy ligand of 0.505 and 0.495 site occupancy, respectively, at general positions were observed as an asymmetric unit. All non-hydrogen atoms were refined anisotropically; the hydrogen atoms were assigned isotropic displacement coefficients U(H) = 1.2U (C), and their coordinates were allowed to ride on their respective atoms. The least-squares refinement of the structural model was performed under geometry restraints and displacement parameter restraints such as DFIX, DANG, ISOR, SIMU and DELU. The final refinement was performed with the modification of the structural factors for the electron densities of the disordered solvents (494 Å^3 (15.6% of the total unit cell volume); 141 electrons correspond to ~14 water molecules per unit cell) using the SQUEEZE option of PLATON.[S3] The carboxylic hydrogen atoms of the $H_{1.5}BTC^{1.5-}$ ligand site were not included in the least-squares refinement. Refinement of the structure converged at a final *R*1 = 0.1364 and *wR*2 = 0.3774 for 2192 reflections with $I > 2\sigma(I)$; *R*1 = 0.1898 and *wR*2 = 0.4123 for all 3954 reflections. The largest difference peak and hole were 1.383 and −0.929 e·Å^{-3}, respectively.

A summary of the crystal data and some crystallography data is given in Tables S1–S4. CCDC-1492751–1492753 and 1536823 contain the supplementary crystallographic data for **3**, **4**, **5**, and **6**. The data can be obtained free of charge at www.ccdc.cam.ac.uk/conts/retrieving.html or from the Cambridge Crystallographic Data Centre, 12 Union Road, Cambridge CB2 1EZ, UK.

Table 1.1. Crystal data and structural refinement for **3**.

Empirical formula	$C_{57}H_{36}NO_{18}Ni_3$	
Formula weight	1353.11	
Temperature	173(2) K	
Wavelength	0.71073 Å	
Crystal system	Monoclinic	
Space group	*Cm*	
Unit cell dimensions	a = 16.384(3) Å	α = 90°
	b = 28.376(6) Å	β = 95.57(3)°
	c = 13.079(3) Å	γ = 90°
Volume	6052(2) $Å^3$	
Z	2	
Density (calculated)	0.743 Mg/m^3	
Absorption coefficient	0.503 mm^{-1}	
F(000)	1380	
Crystal size	0.300 x 0.290 x 0.100 mm^3	
Theta range for data collection	3.005 to 24.000°	
Index ranges	-18<=h<=18, -32<=k<=32, -14<=l<=14	
Reflections collected	18603	
Independent reflections	8954 [R(int) = 0.2363]	
Completeness to theta = 24.000°	99.3 %	
Absorption correction	Semi-empirical from equivalents	
Max. and min. transmission	0.951 and 0.864	
Refinement method	Full-matrix least-squares on F^2	
Data / restraints / parameters	8954 / 542 / 386	
Goodness-of-fit on F^2	1.016	
Final R indices [I>2sigma(I)]	R1 = 0.1322, wR2 = 0.3130	
R indices (all data)	R1 = 0.2243, wR2 = 0.3923	
Absolute structure parameter	0.30(7)	
Largest diff. peak and hole	1.221 and –0.977 $e \cdot Å^{-3}$	

Table 1.2. Crystal data and structure refinement for **4**.

Empirical formula	$C_{57}H_{36}N_{12}O_{18}Ni_3$	
Formula weight	1353.11	
Temperature	173(2) K	
Wavelength	0.700 Å	
Crystal system	Monoclinic	
Space group	*C*2	
Unit cell dimensions	a = 28.676(6) Å	α = 90°
	b = 16.573(3) Å	β = 90.02(3)°
	c = 26.148(5) Å	γ = 90°
Volume	12427(4) $Å^3$	
Z	4	
Density (calculated)	0.723 Mg/m^3	
Absorption coefficient	0.468 mm^{-1}	
F(000)	2760	
Crystal size	0.080 x 0.080 x 0.030 mm^3	
Theta range for data collection	0.767 to 28.997°.	
Index ranges	-39<=h<=39, -21<=k<=21, -36<=l<=36	
Reflections collected	56027	
Independent reflections	32259 [R(int) = 0.1502]	
Completeness to theta = 24.835°	96.5 %	
Absorption correction	Semi-empirical from equivalents	
Max. and min. transmission	0.986 and 0.964	
Refinement method	Full-matrix least-squares on F^2	
Data / restraints / parameters	32259 / 1105 / 721	
Goodness-of-fit on F^2	0.813	
Final R indices [I>2sigma(I)]	R1 = 0.0945, wR2 = 0.2271	
R indices (all data)	R1 = 0.2149, wR2 = 0.2693	
Absolute structure parameter	0.51(2)	
Largest diff. peak and hole	0.599 and –0.645 $e \cdot Å^{-3}$	

Table 1.3. Crystal data and structural refinement for **5**.

Empirical formula	$C_{19}H_{12}N_2O_6Ni$	
Formula weight	423.02	
Temperature	173(2) K	
Wavelength	0.71073 Å	
Crystal system	Hexagonal	
Space group	*P* 6_3/*m c m*	
Unit cell dimensions	a = 16.833(2) Å	α = 90°
	b = 16.833(2) Å	β = 90°
	c = 11.241(2) Å	γ = 120°
Volume	2758.7(10) $Å^3$	
Z	6	
Density (calculated)	1.528 Mg/m^3	
Absorption coefficient	1.094 mm^{-1}	
F(000)	1296	
Crystal size	0.450 x 0.240 x 0.110 mm^3	
Theta range for data collection	3.023 to 27.462°	
Index ranges	–21<=h<=20, –21<=k<=19, –14<=l<=14	
Reflections collected	22841	
Independent reflections	1175 [R(int) = 0.1152]	
Completeness to theta = 25.242°	99.7 %	
Absorption correction	Semi-empirical from equivalents	
Max. and min. transmission	0.889 and 0.639	
Refinement method	Full-matrix least-squares on F^2	
Data / restraints / parameters	1175 / 0 / 83	
Goodness-of-fit on F^2	1.138	
Final R indices [I>2sigma(I)]	R1 = 0.1244, wR2 = 0.2781	
R indices (all data)	R1 = 0.1442, wR2 = 0.2876	
Largest diff. peak and hole	1.745 and –1.833 $e \cdot Å^{-3}$	

Table 1.4. Crystal data and structural refinement for **6**.

Empirical formula	$C_{19}H_{12}N_4O_6Ni$	
Formula weight	451.04	
Temperature	100(2) K	
Wavelength	0.670 Å	
Crystal system	Trigonal	
Space group	*P* -3	
Unit cell dimensions	a = 16.657(2) Å	α = 90°
	b = 16.657(2) Å	β = 90°
	c = 13.173(3) Å	γ = 120°
Volume	3165.4(11) $Å^3$	
Z	6	
Density (calculated)	1.420 Mg/m^3	
Absorption coefficient	0.816 mm^{-1}	
F(000)	1380	
Crystal size	0.040 x 0.040 x 0.008 mm^3	
Theta range for data collection	2.305 to 23.961°	
Index ranges	–20<=h<=20, –20<=k<=20, –15<=l<=15	
Reflections collected	21617	
Independent reflections	3954 [R(int) = 0.1127]	
Completeness to theta = 23.703°	99.7 %	
Absorption correction	Semi-empirical from equivalents	
Max. and min. transmission	0.993 and 0.968	
Refinement method	Full-matrix least-squares on F^2	
Data / restraints / parameters	3954 / 192 / 351	
Goodness-of-fit on F^2	1.422	
Final R indices [I>2sigma(I)]	R1 = 0.1364, wR2 = 0.3774	
R indices (all data)	R1 = 0.1898, wR2 = 0.4123	
Largest diff. peak and hole	1.383 and –0.929 $e \cdot Å^{-3}$	

1.3 RESULTS AND DISCUSSION

Preparation of non-interpenetrated MOFs. *De novo* solvothermal reaction of $Ni(NO_3)_2 \cdot 6H_2O$ and H_3BTC in the presence of the pillaring ditopic linker bipy in DMF solvent led to the formation of [Ni(HBTC)(bipy)]-hms (**1**) with **hms** topology.[31,32] [Ni(HBTC)(bipy)]-gra (**2**) with **gra** topology can be obtained post-synthetically by exchanging the pillaring ligand of [Ni(HBTC)(pz)]-gra, which possesses **gra** topology.[33] [Ni(HBTC)(azpy)]-hms (**3**) with **hms** topology was prepared via a similar procedure to that used for the preparation of **1** with **hms** topology, but using azpy, which is slightly longer than bipy, as a pillaring ligand in a mixed solvent (DMF/MeOH). As shown in Figures 1a and 1b, single crystal structure analysis shows that **3** is a 3D MOF based on 2D sheets pillared via the metal ions by ditopic linkers. **3** is isoreticular to **1**, with (3,5)-c **hms** topology. The 2D sheets with 3-c **hcb** topology in **3** consist of two different 3-c nodes, one based on metal ions and the other based on the organic ligand HBTC, as was the case for the 2D sheet in **1**. While the sheets in **1** are pillared by bipy linkers, the sheets in **3** are pillared by azpy linkers. The bulk identity of the sample was confirmed by comparing the observed powder X-ray diffraction (PXRD) pattern of as-synthesized **3** with the simulated PXRD pattern of the single-crystal structure model of **3** (Figure 2). [Ni(HBTC)(azpy)]-gra (**4**) with **gra** topology was prepared in a similar manner to that used for the preparation of **3** with **hms** topology, but using DMF as the only solvent. As shown in Figures 1c and 1d, single crystal structure analysis shows that **4** is also a 3D MOF based on 2D sheets pillared via the metal ions by ditopic linkers. However, while the pillared 2D sheets in **3** are stacked in an eclipsed fashion (Figure 1a), the pillared 2D sheets in **4** are stacked in a staggered fashion (Figure 1c). **4** is isoreticular to **2**, with (3,5)-c **gra** topology.

The PXRD pattern of **4** with **gra** topology at ambient temperature is similar to but not the same as that of **3** with **hms** topology (Figure 2), with the former showing additional diffraction peaks at 2θ = 11.2° and 14.6°. The peaks marked with an * asterisk in the PXRD pattern of as-synthesized **4** are (*h k l*) reflections with odd *l* indices. The reflections with odd *l* indices are only observed in the structural

model with **gra** topology and a *c*-axis distance of 26.148(5) Å, which is twice of the *c*-axis distance of **3** with **hms** topology, 13.079(3) Å.

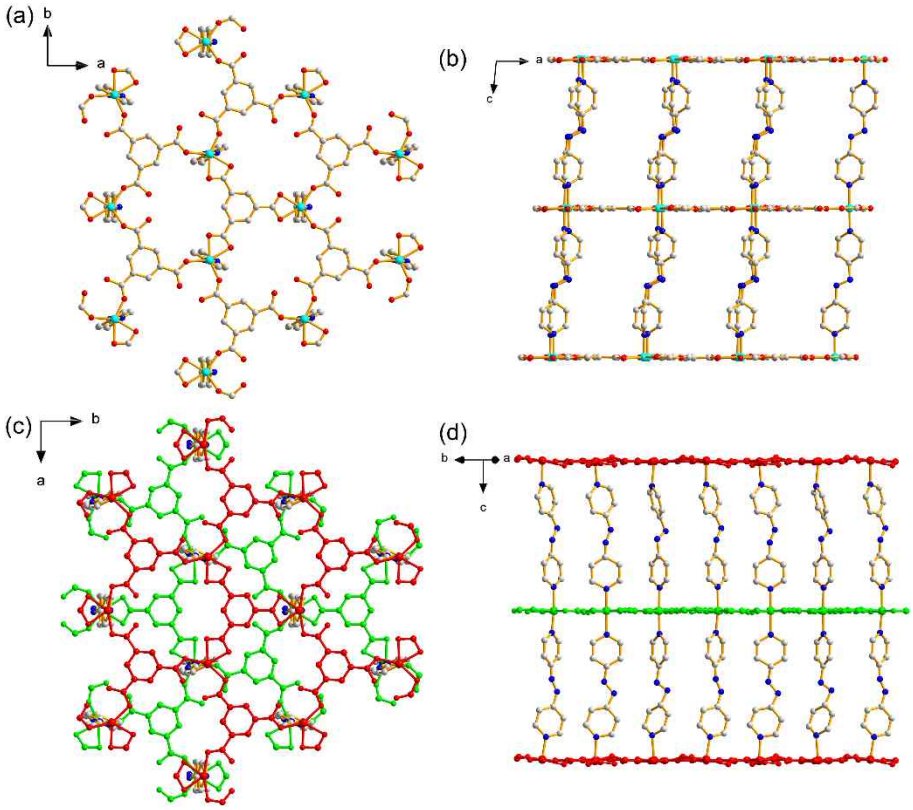

Figure 1.1. Ball-and-stick diagrams of the single crystal structure of **3** with (3,5)-c **hms** topology in (a) top and (b) side view. Ball-and-stick diagrams of the single crystal structure of **4** with (3,5)-c **gra** topology in (c) top and (d) side view. The red and green balls and sticks in (c) and (d) represent the two alternating 2D sheets in the framework with **gra** topology.

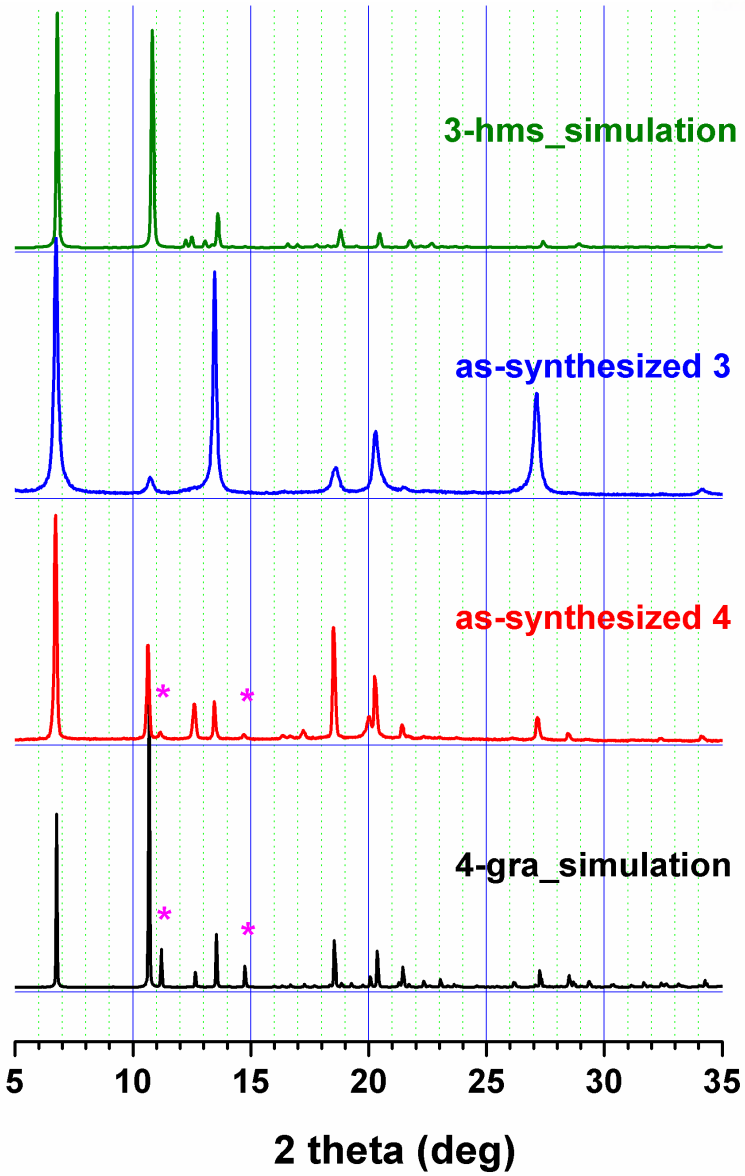

Figure 1.2. Comparison of the PXRD patterns of as-synthesized **3** with **hms** topology and as-synthesized **4** with **gra** topology. The peaks marked with an * asterisk in the PXRD pattern of as-synthesized **4** are (*h k l*) reflections with odd *l* indices.

Gas sorption behavior of the non-interpenetrated MOFs, 3a and 4a. The N_2 sorption behaviors of activated **3 (3a)** and activated **4 (4a)** were similar to the reported behaviors of activated **1 (1a)** and activated **2 (2a)**,[31-33] where the activated MOFs were prepared by presoaking the as-synthesized MOFs in MC then vacuuming them at ambient temperature for 1 d. The N_2 adsorption isotherms of both **3a** and **4a** at 77 K are typical type I plots (Figure 1.3), which confirms the microporosity of both frameworks. The specific pore volume of **3a** as estimated from the uptake amount (495 cm^3/g at 0.97 P/P_0) was 0.765 cm^3/g, which is slightly lower than the calculated specific pore volume of **3** from the single crystal structure, 0.865 cm^3/g. The Brunauer-Emmett-Teller surface area (BET surface area)[40,41] of **3a** as calculated using P/P_0 between 0.0004 and 0.0322 was 1953 m^2/g (Figure 1.4). The specific pore volume of **4a** as estimated from the uptake amount (486 cm^3/g at 0.98 P/P_0) was 0.751 cm^3/g, which is similar to that of **3a**. The BET surface area calculated using the adsorption isotherm data of P/P_0 between 0.00004 and 0.0428 was 1861 m^2/g (Figure 1.5). The pore size analyses of **3a** and **4a** using non-localized density functional theory[42] indicate that they have a similar average pore dimensions but different distributions (Figure 1.6).

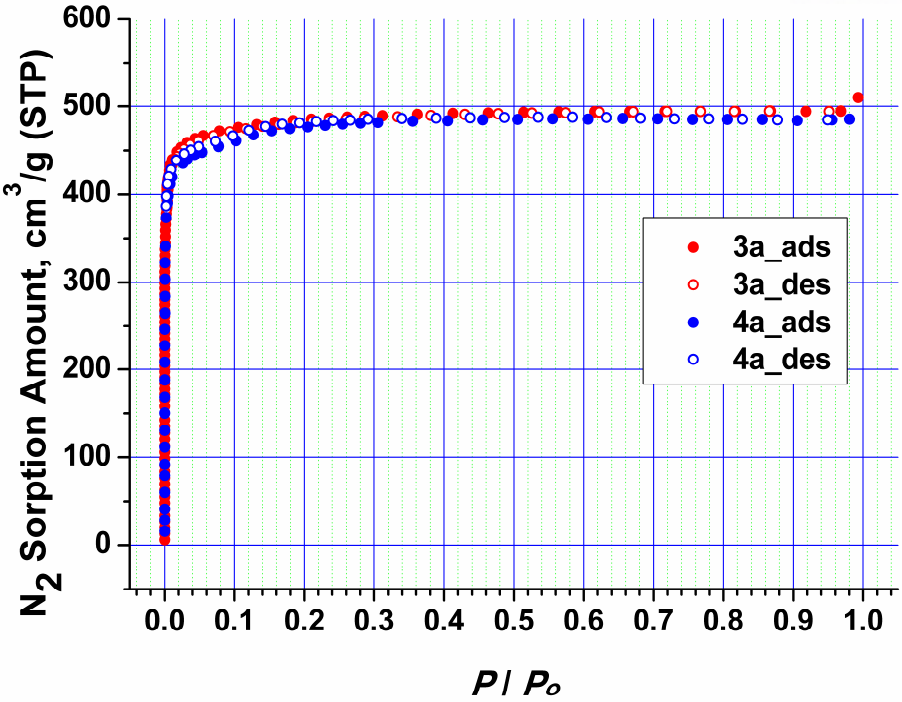

Figure 1.3. N_2 sorption isotherms of **3a** and **4a** at 77 K.

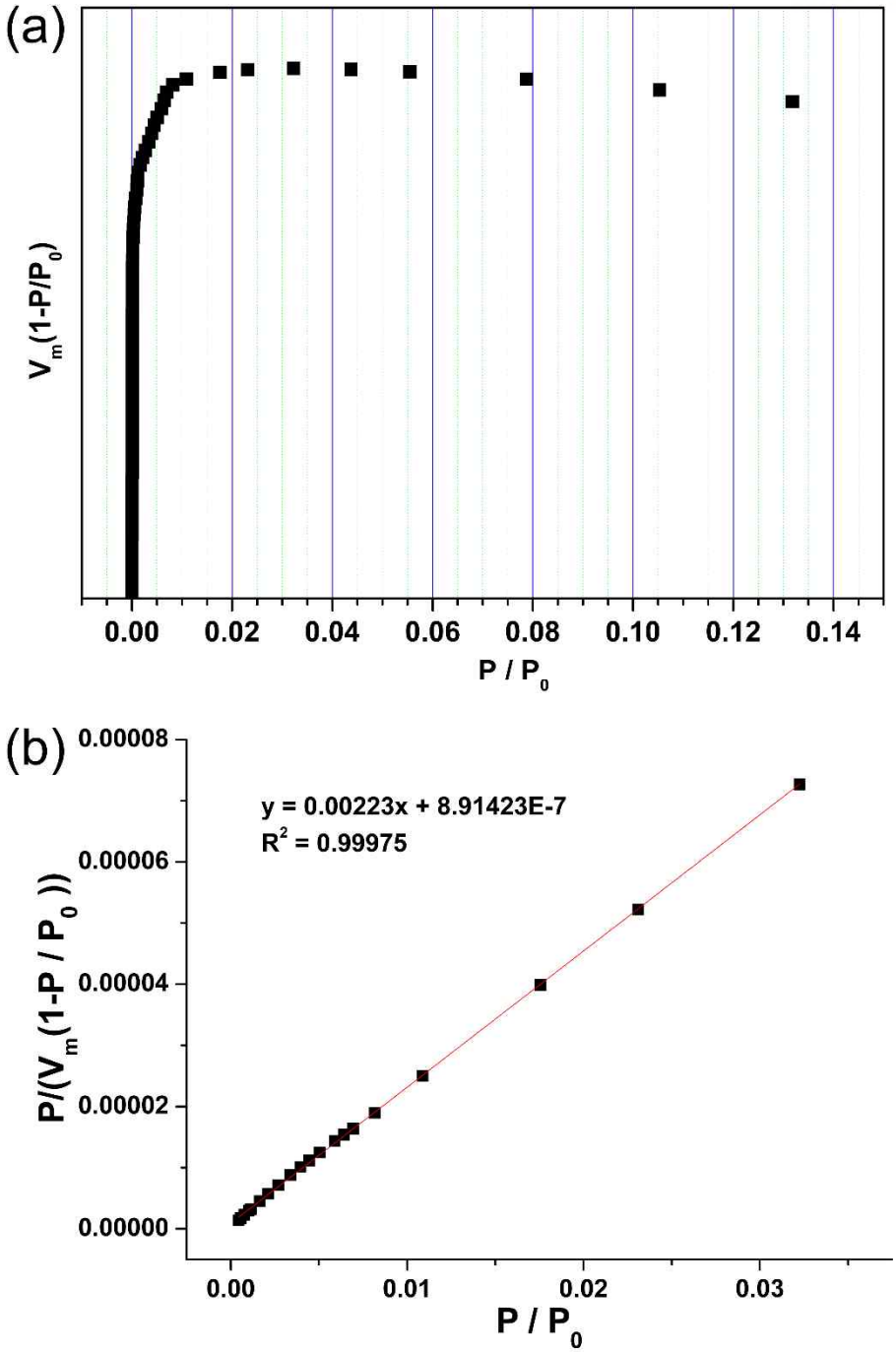

Figure 1.4. BET surface area calculation of **3a**. (a) $V(1 - P/P_0)$ vs. P/P_0 plot. (b) $P/(V_m(1 - P/P_0))$ vs. P/P_0 plot.

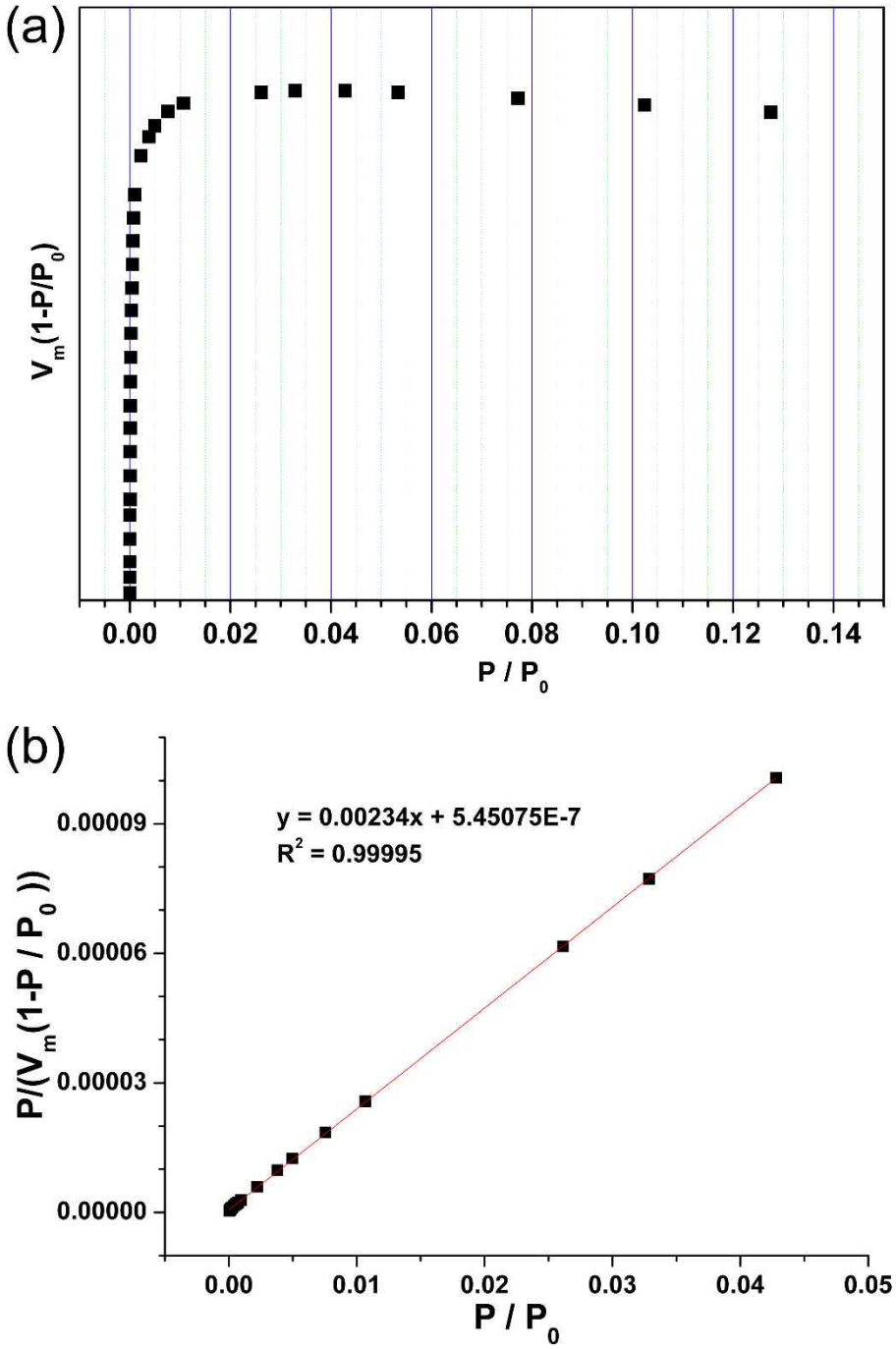

Figure 1.5. BET surface area calculation of **4a**. (a) $V(1 - P/P_0)$ vs. P/P_0 plot. (b) $P/(V_m(1 - P/P_0))$ vs. P/P_0 plot.

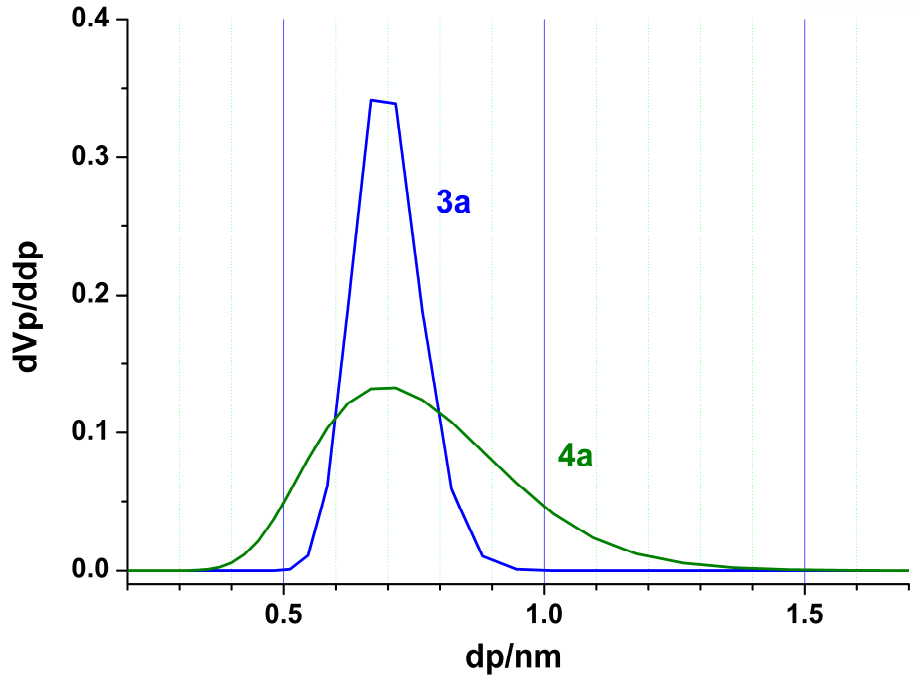

Figure 1.6. Pore size distributions of **3a** and **4a**.

Thermal properties of the non-interpenetrated MOFs. We measured the PXRD patterns of the non-interpenetrated MOFs, **1**-**4**, at several points while increasing temperature of the MOFs under flowing N_2 to observe their thermal stabilities and structural conversions. The temperature-dependent PXRD patterns of as-synthesized **1** indicate that it was stable up to 350 °C and lost its crystallinity at 400 °C (Figure 1.7). Careful examination of the PXRD patterns shows that most diffraction peaks were slightly broadened as the temperature increased up to ~200 °C. However, some peaks, such as those at ~15.8° and ~18.5°, were sharpened again at around 300–350 °C, while the other peaks as the peaks at ~8° and ~23.8° disappeared at around the same temperature. This indicates that **1** converted to a new crystalline phase at around 300 °C. The thermal behavior of **2** with **gra** topology was similar to that of **1** with **hms** topology (Figure 3b). The temperature-dependent PXRD patterns of as-synthesized **2** also show that **2** converted to the same new crystalline phase at around 300 °C via similar broadening. The PXRD pattern of the new phase is similar to but distinctively different from those of both **1** and **2**.

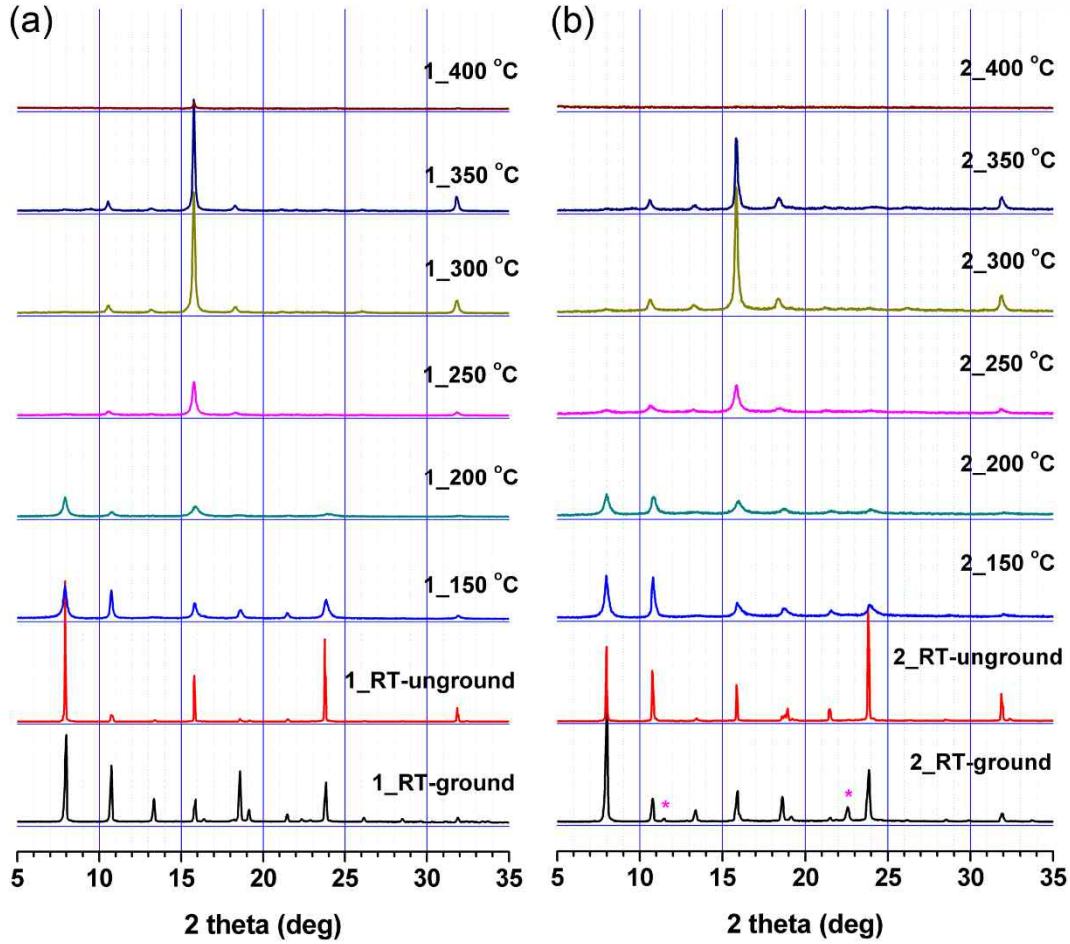

Figure 1.7. Temperature-dependent PXRD patterns of (a) as-synthesized **1** and (b) as-synthesized **2**. The peaks marked with asterisks in the PXRD pattern of as-synthesized **2** are (*h k l*) reflections with odd *l* indices.

The thermal behavior of as-synthesized **3** and as-synthesized **4** were similar to those of as-synthesized **1** and as-synthesized **2**. The temperature-dependent PXRD patterns of as-synthesized **3** and as-synthesized **4** show that the both crystals also maintained their crystallinity up to 350 °C (Figure 4). The diffraction peaks broadened at ~100 °C, much lower than the broadening temperatures of as-synthesized **1** and as-synthesized **2**, but some of them either sharpened or disappeared as the temperature was increased further. As was the case for the temperature-dependent PXRD patterns of as-synthesized **1** and as-synthesized **2**, the PXRD patterns of as-synthesized **3** and as-synthesized **4** also converted to

the same new crystalline phase at around 250 °C, which is distinctively different from the PXRD patterns of either as-synthesized **3** or as-synthesized **4**.

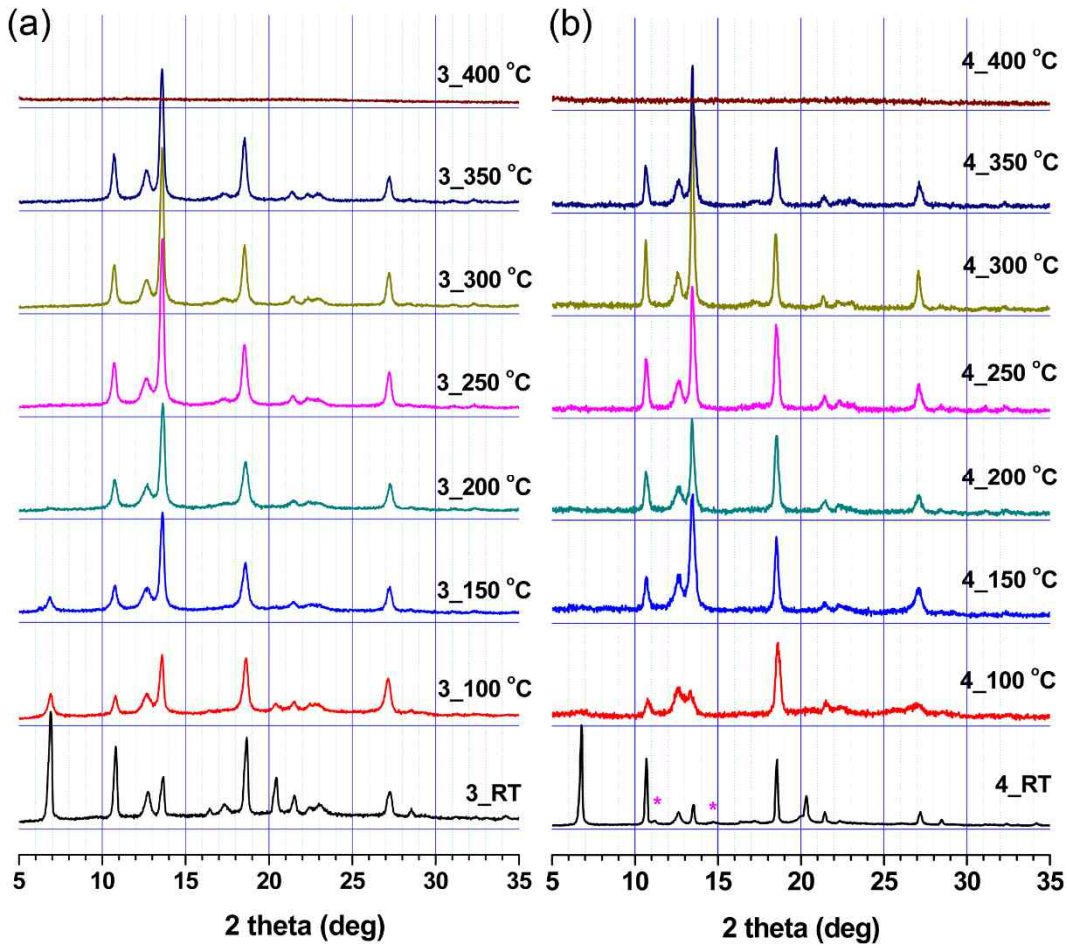

Figure 1.8. Temperature dependent PXRD patterns of as-synthesized **3** and as-synthesized **4**. The peaks marked with asterisks in the PXRD pattern of as-synthesized **4** are (*h k l*) reflections with odd *l* indices, which do not appear in the simulated pattern of **3** with **hms** topology but appear in the simulated pattern of **4** with **gra** topology.

Conversion of non-interpenetrated MOFs to corresponding interpenetrated MOFs. Regardless of their net topologies and pillars, the non-interpenetrated MOFs **1**-**4** can be transformed to the corresponding interpenetrated MOFs with **hms-c** topology, **5** and **6**, by thermal treatment. **1** and **2** were transformed to the same new crystalline phase, [Ni(HBTC)(bipy)]-hms-c (**5**). Single crystals of **5** can be obtained by heating either as-synthesized **1** with **hms** topology or as-synthesized **2** with **gra** topology at 300 °C under flowing N_2. Single crystal structure analysis revealed that **5** consisted of twofold interpenetrated [Ni(HBTC)(bipy)] with **hms-c** topology (Figure 1.9). The structure of a single network is indistinguishable from the framework structure of **1**, the non-interpenetrated [Ni(HBTC)(bipy)] with **hms** topology. 2D layers with **hcb** topology are stacked in an eclipsed fashion with an interlayer distance of 11.2 Å and are pillared by bipy linkers (Figures 1.9). The twofold interpenetration generates two different disc-shaped pores, an A-type cage (6.5 Å in diameter × 2.2 Å in height) and a B5-type cage (7.3 Å in diameter × 2.2 Å in height), in a 2:1 ratio (Figure 1.10). B-type cages have no meaningful portals and are surrounded by six A-type cages in the crystallographic *ab*-plane, while the A-type cages are interconnected via small portals (3.0 Å × 2.2 Å) in the same plane to form 2D porous channels. The void volume of the structure (585 $Å^3$, 21.2% of the total unit cell volume) is significantly reduced compared to those of the corresponding non-interpenetrated analogues.

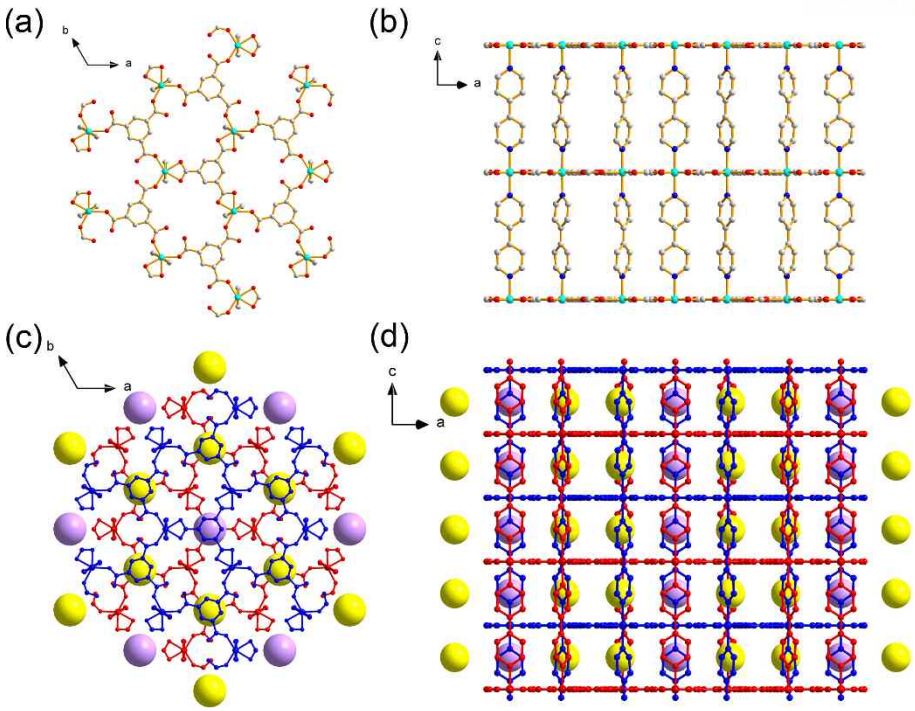

Figure 1.9. Single crystal structure of **5** with **hms-c** topology. (a) Top and (b) side views of a single network with **hms** topology. (c) Top and (d) side views of a twofold interpenetrated network with **hms-c** topology. In (c) and (d), the two interpenetrated networks are represented in red and blue, respectively. The yellow and pink dummy balls in (c) and (d) represent the locations of two different types of cage-like pores in the structure.

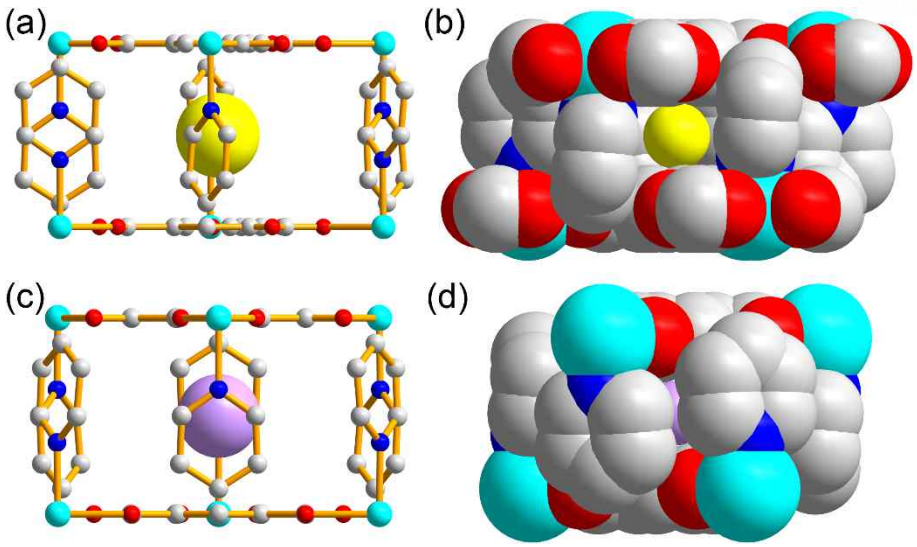

Figure 1.10. (a) Ball-and-stick drawing of an A-type cage in **5** viewed along the [0 1 0] direction and (b) a space-filling drawing of an A-type cage viewed along the [1 -1 0] direction. (c) Ball-and-stick drawing of a B-type cage in **5** viewed along the [0 1 0] direction and (d) a space-filling drawing of a B-type cage viewed along the [1 -1 0] direction. The yellow and pink dummy balls in the centers of the cages represent the inner cavities of the cages.

The other new crystalline phase, [Ni(HBTC)(azpy)]-hms-c (**6**), was obtained via similar thermal treatment of either as-synthesized **3** with **hms** topology or as-synthesized **4** with **gra** topology, using a slightly lower temperature than that used for the preparation of **5** (250 °C compared to 300 °C). **6** is isoreticular to **5** (Figure 1.11), with the 2D layers in **6** being stacked in the same eclipsed fashion as those in **5** and pillared by azpy linkers with an interlayer distance of 13.2 Å (Figures 1.12). Even though the azpy pillars are statistically disordered, the twofold interpenetration again generates two different types of disc-shaped pores, albeit with slightly larger heights in their cavity dimensions compared to those in **5** due to the slightly longer pillars in **6**: A-type cages (6.7 Å in diameter × 3.1 Å in height) and B-type cages (6.4 Å in diameter × 3.1 Å in height) (Figure 1.12). B-type cages have no meaningful portals and are surrounded by six A-type cages in the crystallographic *ab*-plane, while the A-type cages

are interconnected to form 2D porous channels via more flexible portals of similar dimensions (1.7 Å × 3.1 Å) to those in **5**. The potential pore volume of the structure (717 $Å^3$, 22.7% of the total unit cell volume) is again significantly reduced compared to those of the corresponding non-interpenetrated analogues.

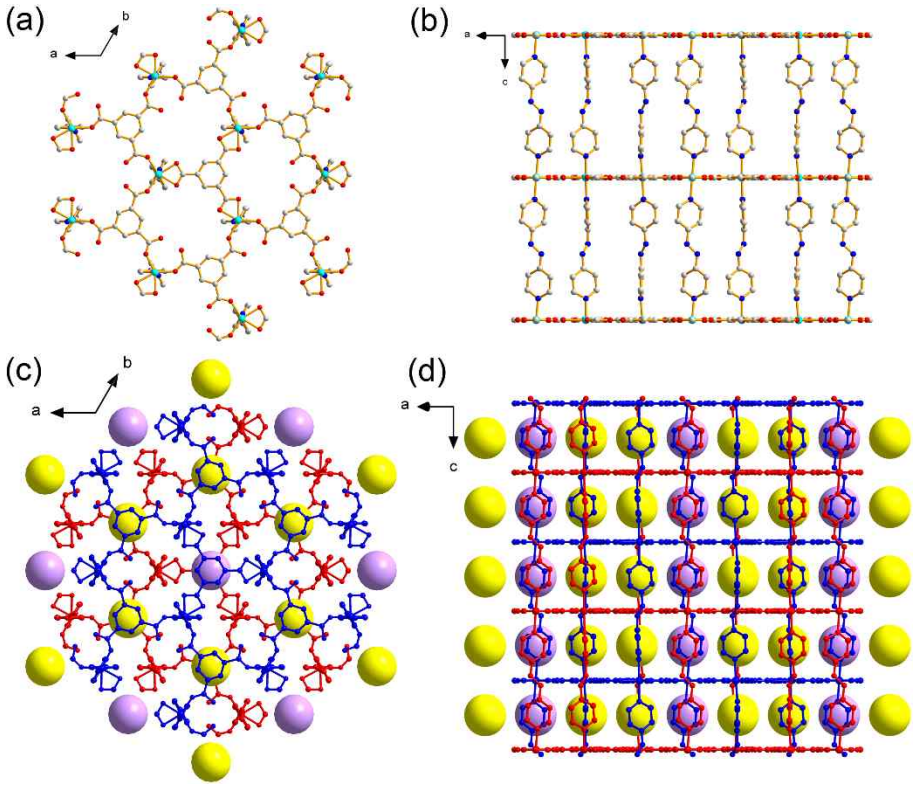

Figure 1.11. Single crystal structure of **6** showing a 3D network of **hms-c** topology. (a) Top-down view of a single network of **hms** topology viewed along the crystallographic *c*-axis. (b) Side view of a single network of **hms** topology viewed along the crystallographic *b*-axis. (c) Side and (d) top-down view of a twofold interpenetrated network of **hms-c** topology. In (c) and (d), the two interpenetrated networks are represented in red and blue, respectively. The yellow and pink dummy balls in (c) and (d) represent the locations of two different types of cage-like pores in the structures.

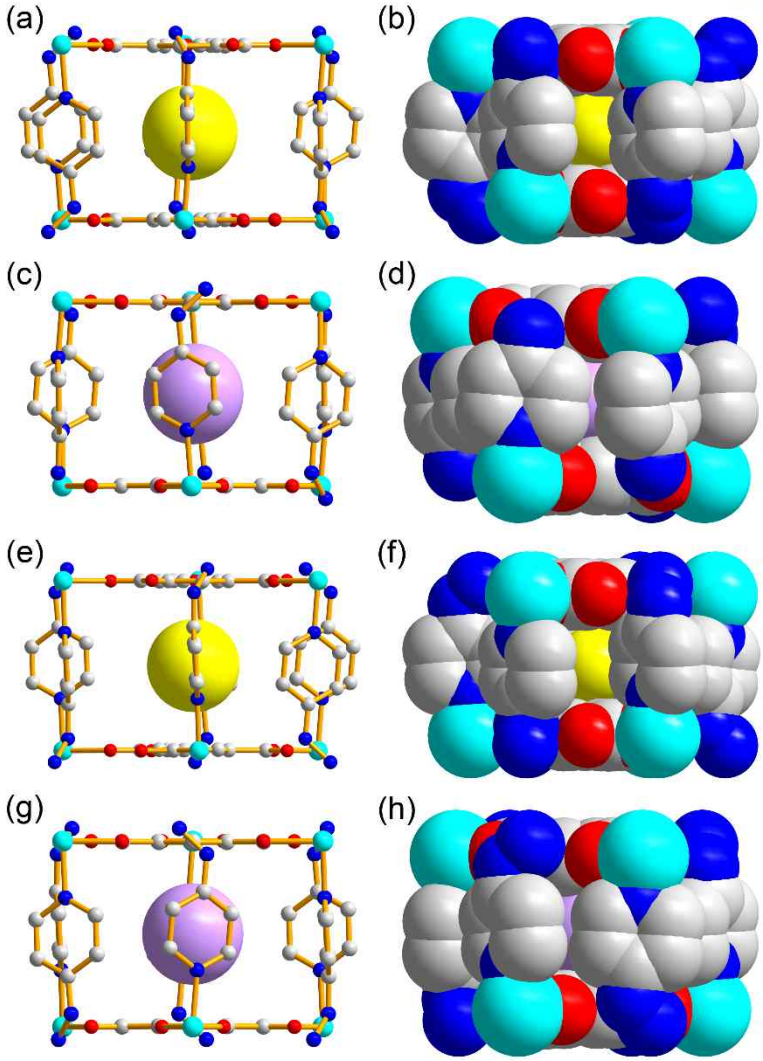

Figure 1.12. (a) (a) Ball-and-stick drawing of an A-type cage in **6** with one of the two statistically disordered azpy pillars viewed along the [0 1 0] direction, and (b) a space-filling drawing of the A-type cage viewed along the [1 -1 0] direction. (c) Ball-and-stick drawing of a B-type cage in **6** with the same statistically disordered azpy pillars viewed along the [0 1 0] direction, and (d) a space-filling drawing of the B-type cage viewed along the [1 -1 0] direction. (e)–(h) The corresponding drawings of the cages in **6** with the other statistically disordered azpy pillar to that shown as the drawings in (a)–(d). The yellow and pink dummy balls in the centers of the cages represent the inner cavities of the cages.

Structural conversion with no solvent assistance. Solvent-assisted linker exchange (SALE) (which

is also known as post-synthetic ligand exchange (PSLE)) requires solvent participation in the formation and stabilization of either intermediates or transition states during the structural conversion.[43-46] Conversion of non-interpenetrated MOFs to corresponding interpenetrated MOFs requires bond dissociation and re-association; however, this structural conversion can occur without solvent assistance. Thermal treatment of the non-interpenetrated MOFs led to the corresponding twofold interpenetrated MOFs both before and after the complete removal of the solvent from the pores (Figure 1.13). The complete removal of the solvents from the non-interpenetrated MOFs was confirmed from using the ^{1}H NMR spectra of **1'** and **3'**, which were prepared by drying as-synthesized **1** and as-synthesized **3**, respectively, that had been presoaked in MC at 150 °C for 30 min under flowing N_2, then digested in d_6-DMSO/DCl or D_2O/DCl (Figure 1.14). No proton peaks from DMF or MC molecules were observed in the ^{1}H NMR spectra. The thermal energy at 250–300 °C is high enough for the activation of the metal centers of the frameworks, allowing successful structural conversions via either unstable intermediates or transition states without solvent assistance.

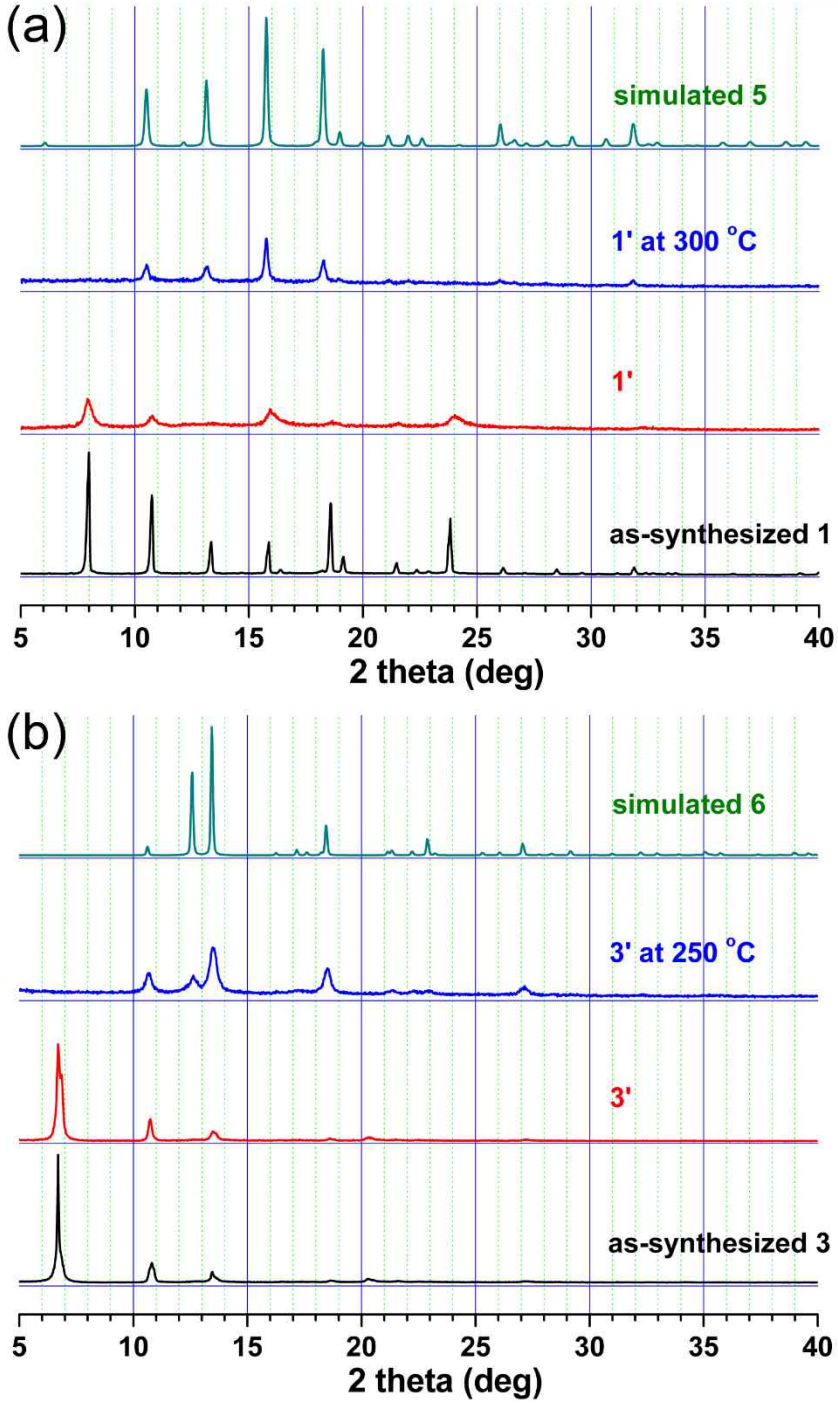

Figure 1.13. (a) PXRD patterns of **1'** and **1'** treated at 300 °C for 30 min under flowing N_2. (b) PXRD patterns of **3'** and **3'** treated at 250 °C for 30 min under flowing N_2.

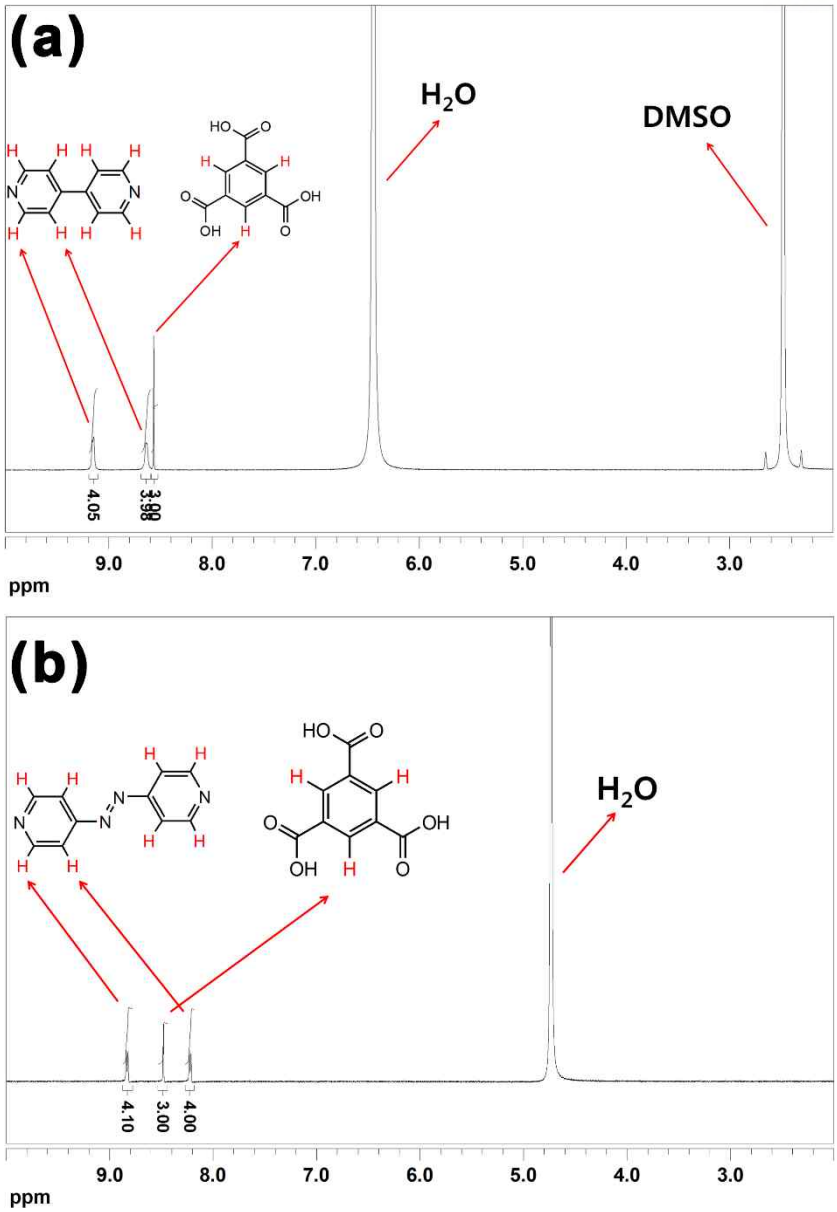

Figure 1.14. (a) ^{1}H NMR spectrum of **1'** in d_6-DMSO/DCl, where **1'** was prepared by drying **1** presoaked in methylene chloride at 150 °C for 30 min under flowing N_2. (b) ^{1}H NMR spectrum of **3'** in D_2O/DCl, where **3'** was prepared by drying **3** presoaked in methylene chloride at 150 °C for 30 min under flowing N_2.

Conversion mechanisms. The conversion of a non-interpenetrated network based on pillared 2D layers into a corresponding twofold interpenetrated network must be accomplished via sequential pillar dissociation, structural reorganization, and pillar re-association (Scheme 1.2). The pillars in **2** (or **4**) with **gra** topology must be either fully or partially dissembled from the 2D layers for the network conversion. Then, the 2D layers need to be reorganized to staggered stacked layers via layer translation, followed by layer contraction. Finally, the stacked 2D layers must be reassembled with pillars into doubly interpenetrated **5** (or **6**) with **hmc-c** topology. The conversion to a doubly interpenetrated MOF with **gra-c** topology is not observed since such a conversion would require layer rotation, which is energetically the more demanding than layer translation. Even successful layer rotation will lead to either collision or at least severe steric repulsion between interpenetrated networks with **gra-c** topology. While the conversion of a MOF with **gra** topology to a doubly interpenetrated MOF with **hmc-c** topology can proceed via the less energetically demanding layer translation, the conversion from non-interpenetrated **1** (or **3**) with **hms** topology to doubly interpenetrated **5** (or **6**) with **hms-c** topology cannot proceed via the same layer translation. Such a layer translation would lead to doubly interpenetrated networks with **gra-c** topology, which is again frustrated by the steric repulsion between the interpenetrated networks as described above. Although conversion by layer rotation can lead to doubly interpenetrated networks with **hmc-c** topology, it is not a likely process since such a conversion demands an extremely large amount of energy for the structural reorganization. The network conversion can proceed via localized structural reorganization within a 2D layer. Instead of rotation of a whole 2D layer, localized rotations of the $HBTC^{2-}$ ligands within a 2D layer could lead to a conversion of non-interpenetrated **1** (or **3**) with **hms** topology into doubly interpenetrated **5** (or **6**) with **hms-c** topology. For complete conversion, every $HBTC^{2-}$ ligand of the monodentate binding mode must rotate ~30° in a direction opposite to that of the adjacent $HBTC^{2-}$ ligands of the same monodentate binding mode within a 2D layer. The $HBTC^{2-}$ ligand of the chelating bidentate binding mode must rotate ~60° in any direction within a 2D layer. The localized rotations of the two different types of $HBTC^{2-}$ ligands allow network conversion without extensive structural reorganization that does not lead to collision between the interpenetrated networks.

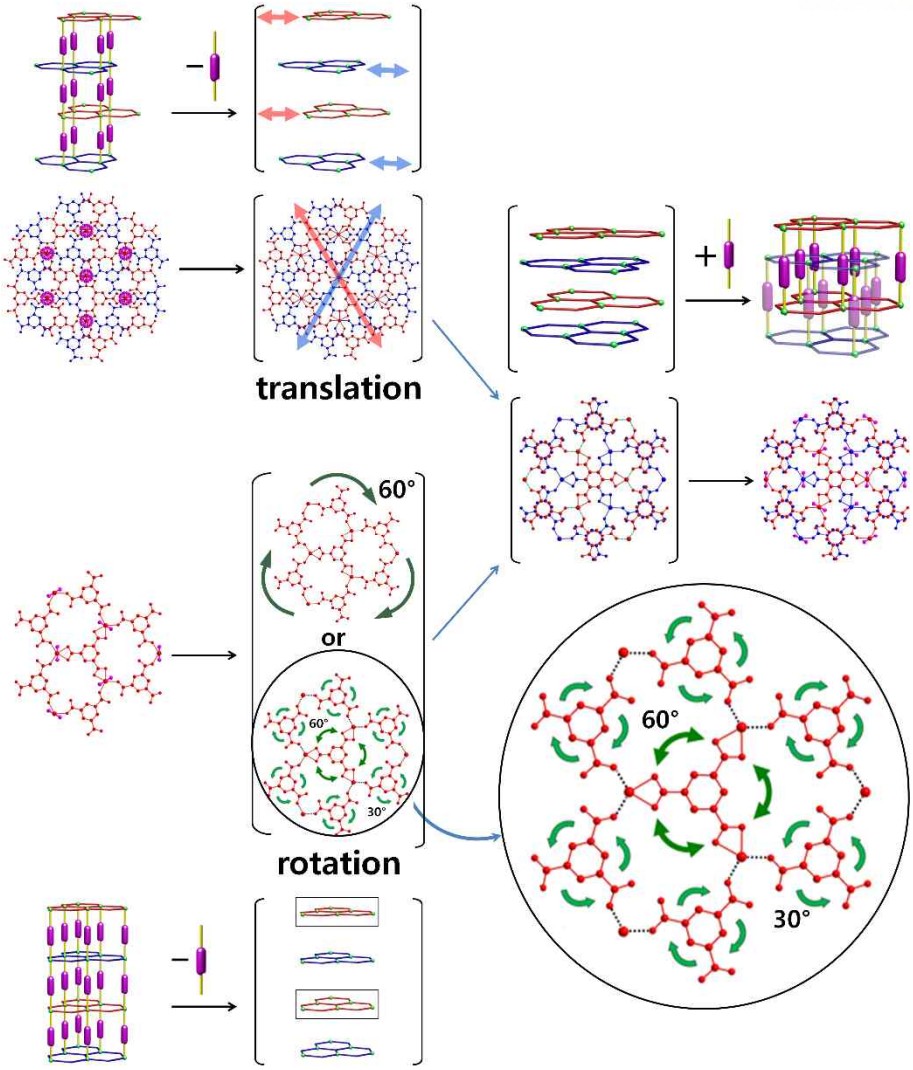

Scheme 1.2. Proposed conversion mechanisms from both non-interpenetrated networks with **hms** topology and with **gra** topology to a doubly interpenetrated network with **hms-c** topology.

Gas sorption behavior of the interpenetrated MOFs, 5a and 6a.

The N_2 sorption of activated **6a** also follows a type I adsorption with some hysteric desorption (Figure 1.15), where activated **6a** was prepared by vacuuming as-synthesized **6** at 100 °C for 3 h. The BET surface area calculated using P/P_0 between 0.00001 and 0.0585 was 392 m^2/g (Figure 1.17), and the N_2 uptake amount at 77 K and 0.98 bar was 132 cm^3/g. The specific pore volume as estimated from the uptake amount was 0.204 cm^3/g, slightly larger than the calculated specific void volume of the single crystal structure model, 0.160 cm^3/g. Even though the single crystal structure of **5** was similar to that of **6**, the N_2 sorption behavior of activated **5a**, prepared by vacuuming as-synthesized **5** at 100 °C for 3 h, was significantly different from that of activated **6a**. The N_2 adsorption isotherm of **5a** shows features of both type I and type IV isotherms simultaneously. The type I feature, a steep rise in the N_2 uptake at very low P/P_0, indicates the presence of micropores. The subsequent slow increase in N_2 uptake up to P/P_0 ~0.86 and the hysteresis loop between P/P_0 0.86 and 0.97 are type IV features of mesoporous materials. The BET surface area of **5a** as calculated using P/P_0 between 0.00002 and 0.0802 was 259 m^2/g (Figure 1.18). The specific pore volume estimated from the uptake amount (495 cm^3/g at 77K and 0.97 bar) was 0.767 cm^3/g, significantly larger that the calculated specific void volume of the single crystal structure model, 0.139 cm^3/g. The pore size analyses of **5a** and **6a** as performed using non-localized density functional theory[36] indicate that the both have two different types of pores, micro- and mesopores (Figure 1.16). **6a** had micropores with an average dimension of ~5.8 Å and mesopores with an average dimension of ~3.7 nm, in approximately a 3:1 volume ratio. The formation of the mesopores was probably due to the partial removal of the neutral azpy pillars during the thermal treatment at 250 °C during the structural conversion of non-interpenetrated **3** to twofold interpenetrated **6**. The $HBTC^{2-}$–to–azpy ratio in the ^1H NMR spectrum of **6a** digested in D_2O/DCl supports the partial removal (~8%) of the neutral azpy pillars from the structure during the thermal treatment (Figure 1.19). The EA result also supports the partial removal (~5%) of the neutral azpy pillars from the structure. **5a** also had micropores with an average dimension of ~5.2 Å and mesopores with an average dimension of ~31 nm, in a volume ratio of approximately 1:6. Both the size and the cumulative volume of the micropores in **5a** were

slightly smaller than the corresponding values for **6a**. In contrast, the dimension and the cumulative volume of the mesopores of **5a** were much larger than the corresponding values for **6a**. Some neutral bipy pillars were also removed from the structure during the thermal treatment at 300 °C for the structural conversion from non-interpenetrated **1** to doubly interpenetrated **5**. Both the ^{1}H NMR spectrum (Figure 1.20) and the EA of **5a** support the partial removal (~8 and ~11%, respectively) of the neutral bipy pillars from the framework during the thermal treatment.

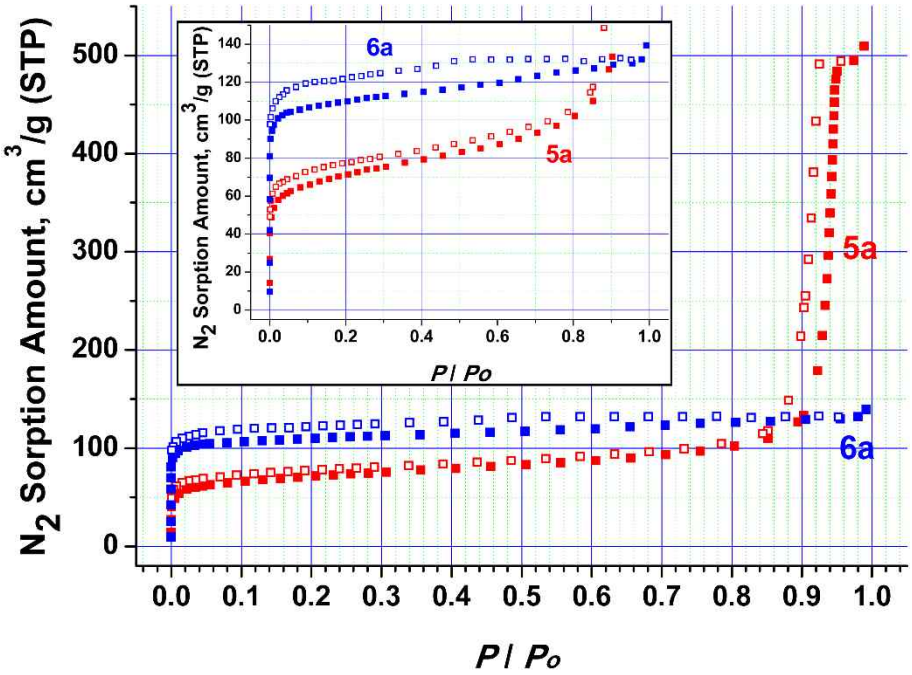

Figure 1.15. The N_2 sorption isotherms of **5a** and **6a** at 77 K. Adsorption and desorption isotherms are represented by filled and empty squares, respectively.

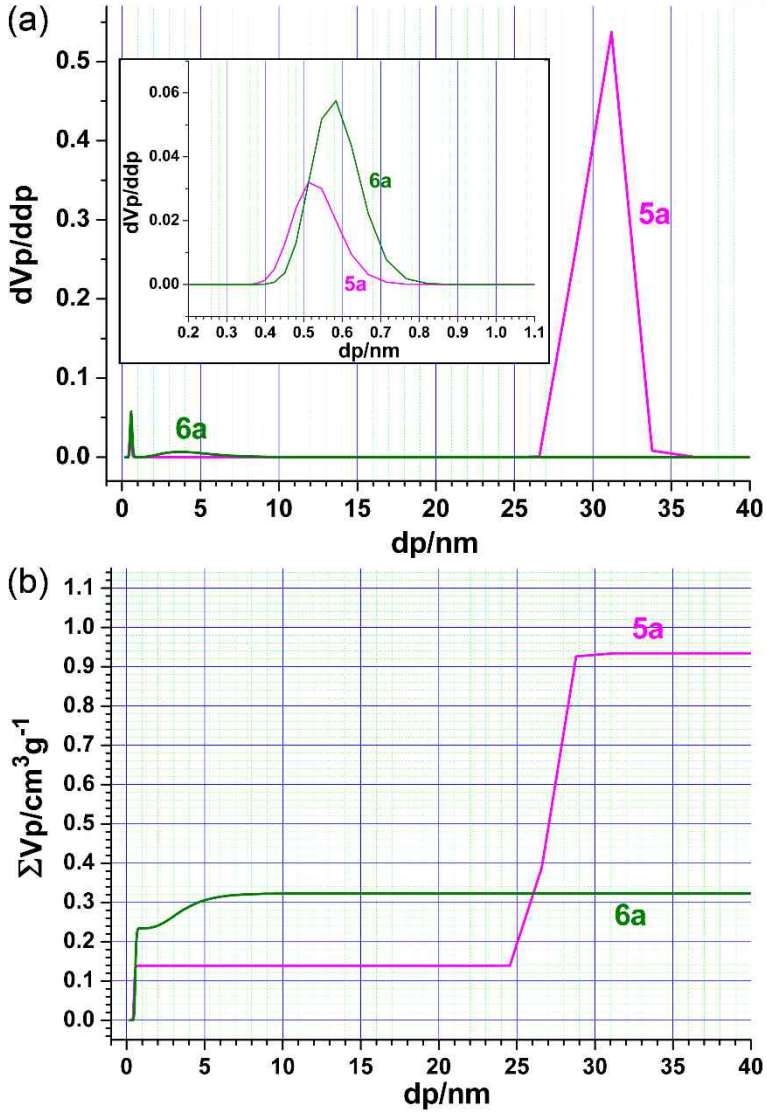

Figure 1.16. (a) Pore size distributions and (b) cumulative pore volumes of **5a** and **6a**.

.

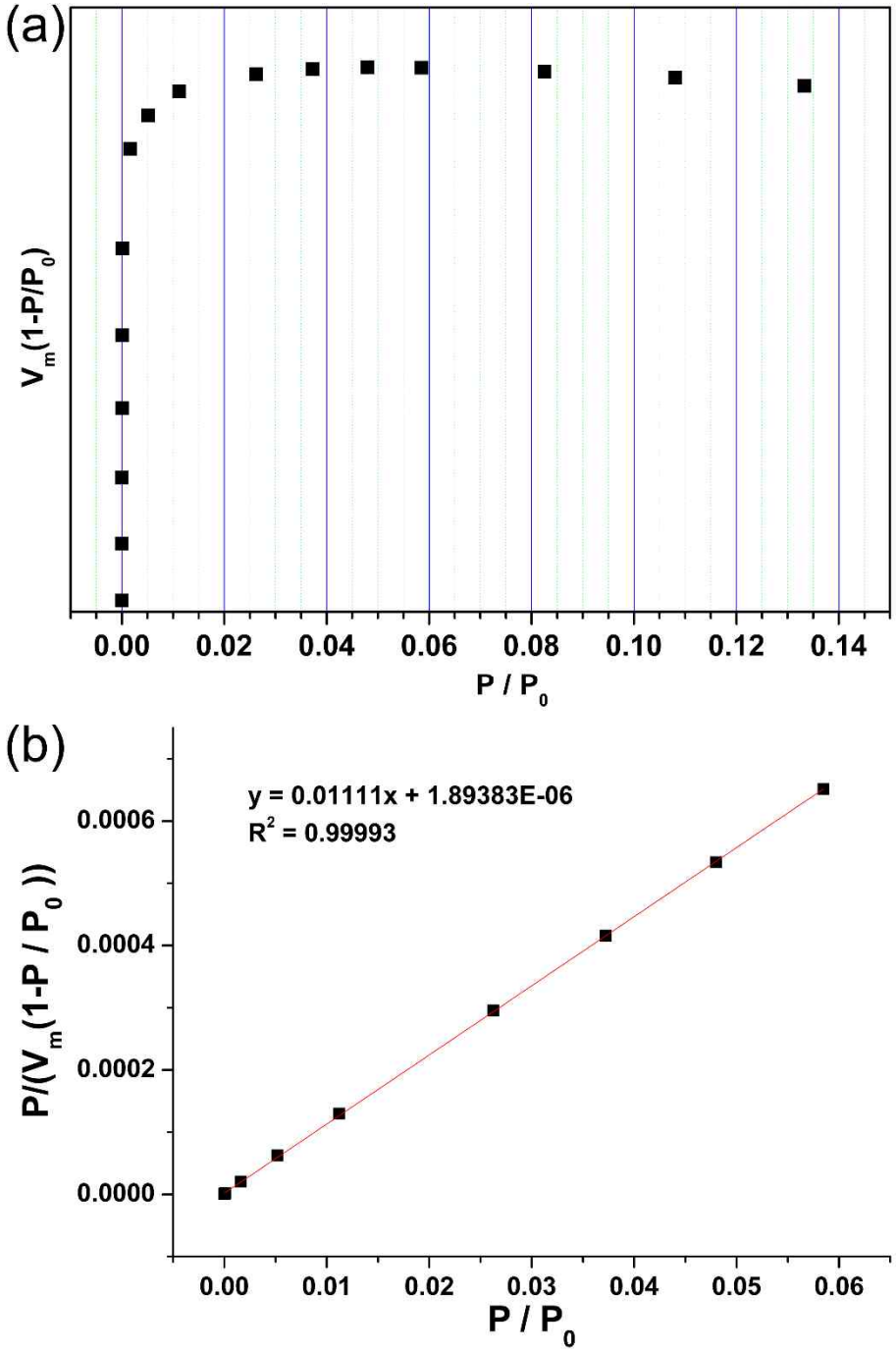

Figure 1.17. BET surface area calculation of **6a**. (a) $V(1 - P/P_0)$ vs. P/P_0 plot. (b) $P/(V_m(1 - P/P_0))$ vs. P/P_0 plot.

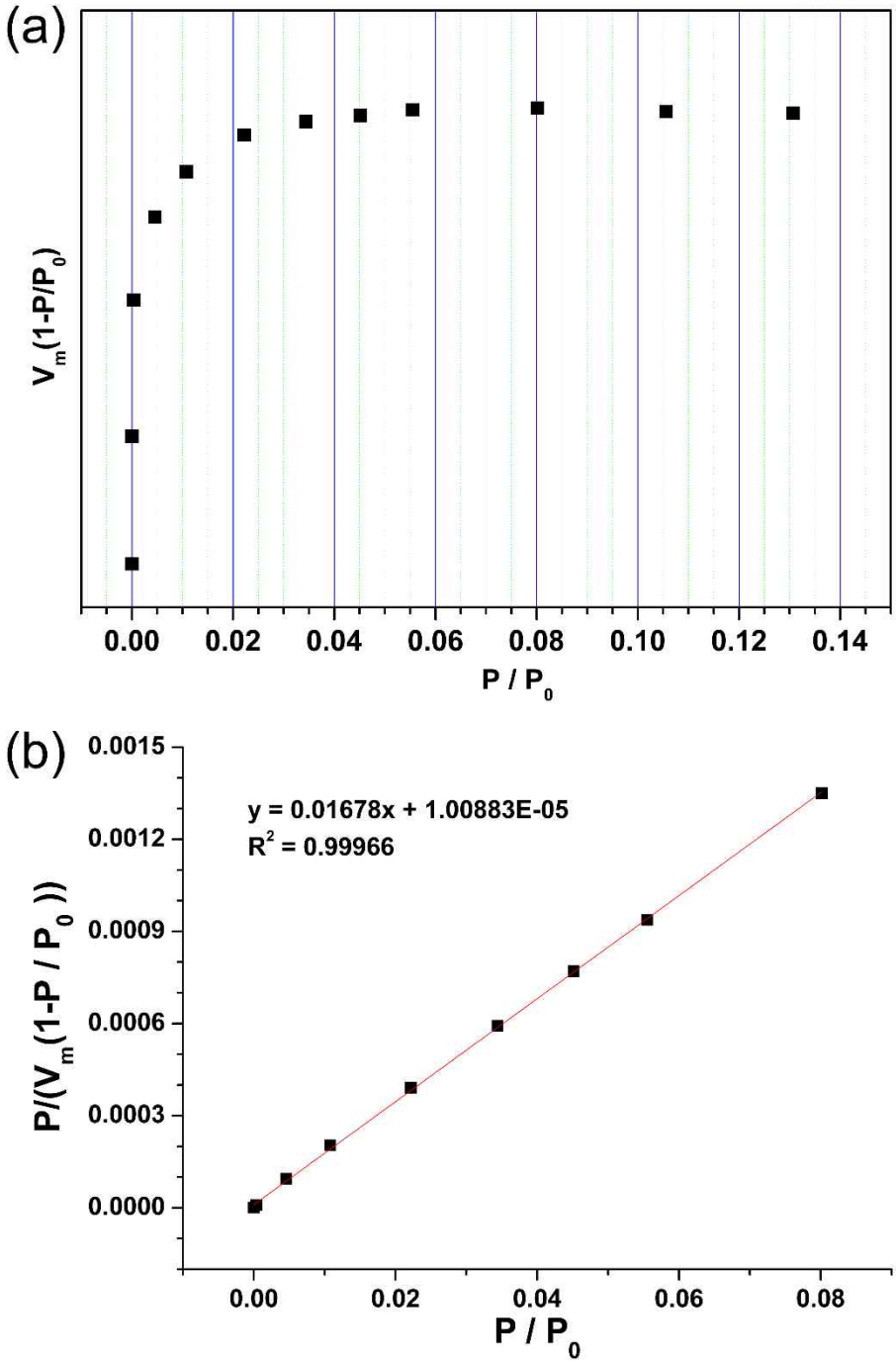

Figure 1.18. BET surface area calculation of **5a**. (a) $V(1 - P/P_0)$ vs. P/P_0 plot. (b) $P/(V_m(1 - P/P_0))$ vs. P/P_0 plot.

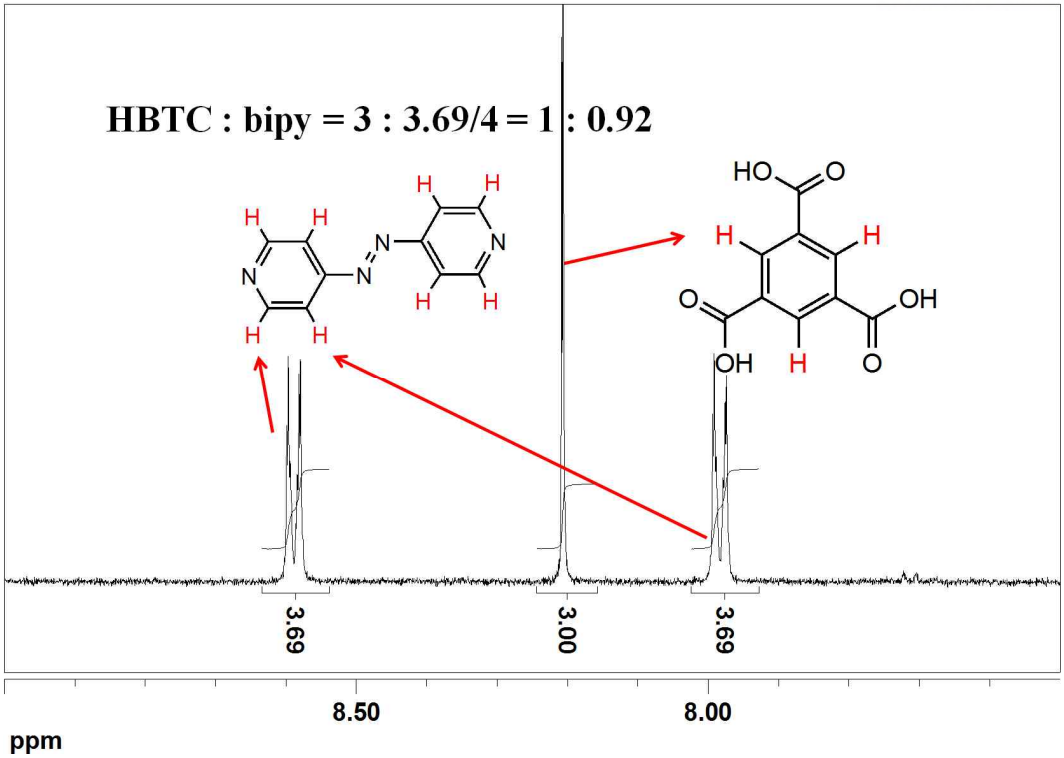

Figure 1.19. ^{1}H NMR spectrum of **6a** digested in D_2O/DCl.

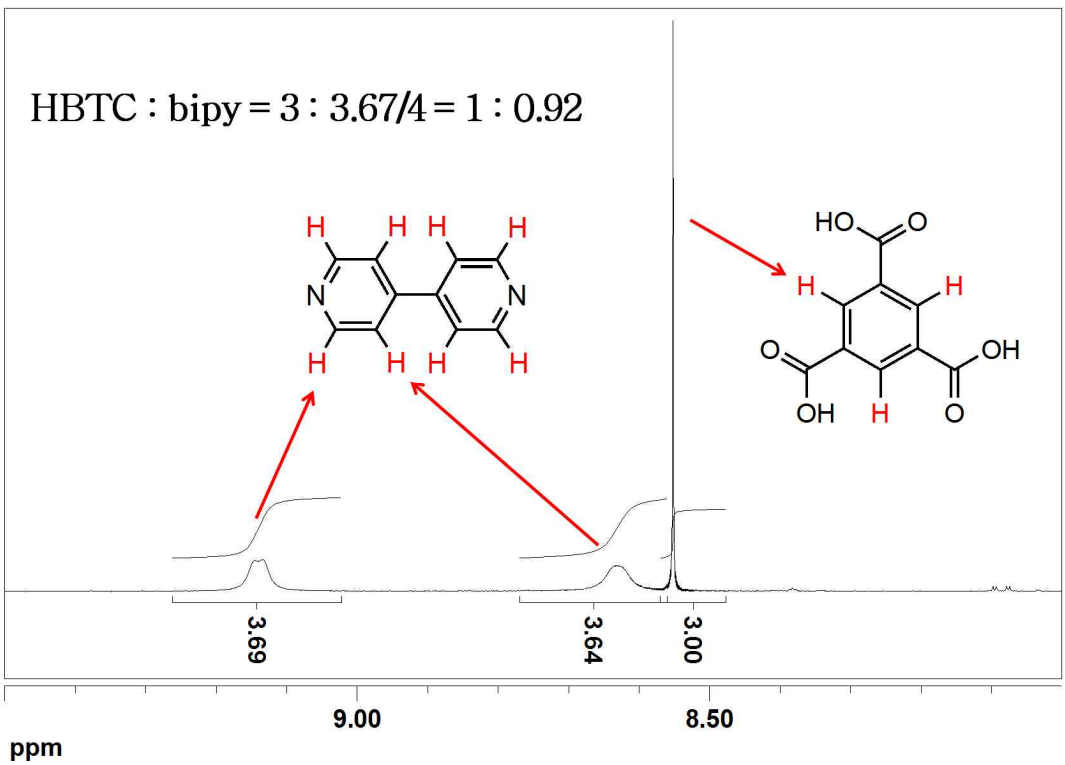

Figure 1.20. ^{1}H NMR spectrum of **5a** digested in d_6-DMSO/DCl.

1.4. CONCLUSIONS

Microporous MOFs with not only interpenetration-favorable (3,5)-c **hms** topology but also with interpenetration-unfavorable (3,5)-c **gra** topology were prepared by either *de novo* solvothermal syntheses or by post-synthetic ligand exchange. Thermal treatment of the less densely packed non-interpenetrated MOFs led to the more densely packed doubly interpenetrated MOFs in SCSC fashion in the solid state, and even in the absence of solvent molecules in the pores. The conversion occurred regardless of the net topologies of the non-interpenetrated MOFs and the pillaring linkers. The conversions of non-interpenetrated MOFs with **gra** topology to the corresponding doubly interpenetrated MOFs with **hms-c** topology occurred via 2D layer translation. In contrast, the conversion from non-interpenetrated MOFs with **hms** topology to the corresponding doubly interpenetrated MOFs with **hms-c** topology occurred via localized rotations of $HBTC^{2-}$ ligands within the 2D layer. Thermal treatment of non-interpenetrated microporous MOFs thermodynamically generated the more stable interpenetrated microporous MOFs. Depending on thermal treatment conditions and the properties of the neutral pillaring linkers, MOFs that contain both micro- and mesopores were generated by partial removal of the neutral pillaring linkers. Non-stoichiometric removal of neutral pillaring linkers from MOFs by thermal treatment could lead to new interpenetrated MOFs that simultaneously contain micro- and mesopores. The pore dimension distributions could be controlled depending on the properties of the pillars and the thermal treatment conditions.

1.5. REFERENCES

(1) Zhou, H.-C.; Kitagawa, S. Metal-organic frameworks (MOFs). *Chem. Soc. Rev.* **2014**, *43*, 5415-5418.

(2) Furukawa, H.; Cordova, K. E.; O'Keeffe, M.; Yaghi, O. M. The chemistry and applications of metal-organic frameworks. *Science* **2013**, *341*, 973-987.

(3) Zhou, H.-C.; Long, J. R.; Yaghi, O. M. Introduction to metal-organic frameworks. *Chem. Rev.* **2012**, *112*, 673-674.

(4) Long, J. R.; Yaghi, O. M. The pervasive chemistry of metal-organic frameworks. *Chem. Soc. Rev.* **2009**, *38*, 1213-121.

(5) Batten, S. R.; Robson, R. Interpenetrating nets: ordered, periodic entanglement. *Angew. Chem. Int. Ed.* **1998**, *37*, 1460-1494.

(6) Carlucci, L.; Ciani, G.; Proserpio, D. M. Polycatenation, polythreading and polyknotting in coordination network chemistry. *Coor. Chem. Rev.* **2003**, *246*, 247-289.

(7) Baburin, I. A.; Blatov, V. A.; Carlucci, L.; Ciani, G.; Proserpio, D. M. Interpenetrating metal-organic and inorganic 3D networks: a computer-aided systematic investigation. Part II [1]. Analysis of the inorganic crystal structure database (ICSD). *J. Solid State Chem.* **2005**, *178*, 2452-2474.

(8) Alexandrov, E. V.; Blatov, V. A.; Kochetkov, A. V.; Proserpio, D. M. Underlying nets in three-periodic coordination polymers: topology, taxonomy and prediction from a computer-aided analysis of the Cambridge Structural Database. *CrystEngComm* **2011**, *13*, 3947-3958.

(9) Bonneau, C.; O'keeffe, M. High-symmetry embeddings of interpenetrating periodic nets. Essential rings and patterns of catenation. *Acta Cryst*. **2015**, A71, 82-91.

(10) O'Keeffe, M.; Peskov, M. A.; Ramsden S. J.; Yaghi1, O. M. The reticular chemistry Structure sesource (RCSR) database of, and symbols for, crystal nets. *Acc. Chem. Res.* **2008**, *41*, 1872-1789.

(11) Blatov, V. A.; Carlucci, L.; Ciani, G.; Proserpio, D. M. Interpenetrating metal–organic and inorganic 3D networks: a computer-aided systematic investigation. Part I. Analysis of the Cambridge structural database. *CrystEngComm* **2004**, *6*, 377-395.

(12) Bonneau, C.; Delgado-Friedrichs, O.; O'Keeffe, M.; Yaghi, O. M. Three-periodic nets and tilings: minimal nets. *Acta Cryst.* **2004**, *A60*, 517-520.

(13) Chae, H. K.; Siberio-Pérez, D. Y.; Kim, J.; Go, Y. B.; Eddaoudi, M.; Matzger, A. J.; O'Keeffe, M.; Yaghi, O. M. A route to high surface area, porosity and inclusion of large molecules in crystals. *Nature* **2004**, *427*, 523-527.

(14) Furukawa, H.; Ko, N.; Go, Y. B.; Aratani, N.; Cho, S. B.; Choi, E.; Yazaydin, A. Ö.; Snurr, R. Q.; O'Keeffe, M.; Kim J.; Yaghi1, O. M. Ultrahigh porosity in metal-organic frameworks. *Science* **2010**, *329*, 424-428.

(15) Zou, Y.; Park, M.; Hong, S.; Lah, M. S. A designed metal-organic framework based on a metal–organic polyhedron. *Chem. Commun.* **2008**, 2340-2342.

(16) Farha, O. K.; Wilmer, C. E.; Eryazici, I.; Hauser, B. G.; Parilla, P. A.; O'Neill, K.; Sarjeant, A. A.; Nguyen, S. T.; Snurr R. Q.; Hupp, J. T. Designing higher surface area metal-organic frameworks: are triple bonds better than phenyls?. *J. Am. Chem. Soc.* **2012**, *134*, 9860-9863.

(17) Rosi, N. L.; Eddaoudi, M.; Kim, J.; O'Keeffe, M.; Yaghi, O. M. Infinite secondary building units and forbidden catenation in metal-organic frameworks. *Angew. Chem. Int. Ed.* **2002**, *41*, 284-287.

(18) Deng, H.; Grunder, S. ; Cordova, K. E.; Valente, C.; Furukawa, H.; Hmadeh, M.; Gándara, F.; Whalley, A. C.; Liu, Z.; Asahina, S.; Kazumori, H.; O'Keeffe, M.; Terasaki, O.; Stoddart, J. F.; Yaghi, O. M. Large-pore apertures in a series of metal-organic frameworks *Science* **2012**, *336*, 1018-1023.

(19) Farha, O. K.; Malliakas, C. D.; Kanatzidis, M. G.; Hupp, J. T. Control over catenation in metal-organic frameworks via rational design of the organic building block. *J. Am. Chem. Soc.* **2009**, *132*, 950-952.

(20) Roberts, J. M.; Farha, O. K.; Sarjeant, A. A.; Hupp, J. T.; Scheidt, K. A. Two azolium rings are better than one: a strategy for controlling catenation and morphology in Zn and Cu metal-organic frameworks. *Cryst. Growth Des.* **2011**, *11*, 4747-4750.

(21) Zhang, J.; Wojtas, L.; Larsen, R. W.; Eddaoudi, M.; Zaworotko, M. J. Temperature and concentration control over interpenetration in a metal-organic material. *J. Am. Chem. Soc.* **2009**, *131*, 17040-17041.

(22) Long, D.-L.; Hill, R. J.; Blake, A. J.; Champness, N. R.; Hubberstey, P.; Wilson, C.; Schröder, M. Anion control over interpenetration and framework topology in coordination networks based on homoleptic six-connected scandium nodes. *Chem. – A Eur. J.* **2005**, *11*, 1384-1391.

(23) Bureekaew, S.; Sato, H.; Matsuda, R.; Kubota, Y.; Hirose, R.; Kim, J.; Kato, K.; Takata, M.; Kitagawa, S. Control of interpenetration for tuning structural flexibility influences sorption properties. *Angew. Chem. Int. Ed.* **2010**, *49*, 7660-7664.

(24) Ma, S.; Sun, D.; Ambrogio, M.; Fillinger, J. A.; Parkin, S.; Zhou, H.-C. Framework-catenation isomerism in metal-organic frameworks and its impact on hydrogen uptake. *J. Am. Chem. Soc.* **2007**, *129*, 1858-1859.

(25) Choi, S. B.; Furukawa, H.; Nam, H. J.; Jung, D.-Y.; Jhon, Y. H.; Walton, A.; Book, D.; O'Keeffe, M.; Yaghi, O. M.; Kim, J. Reversible interpenetration in a metal-organic framework triggered by ligand removal and addition. *Angew. Chem. Int. Ed.*, **2012**, *51*, 8791-8795.

(26) Aggarwal, H.; Lama, P.; Barbour, L. J. Transformation from non- to double-interpenetration in robust Cd(II) doubly-pillared-layered metal–organic frameworks. *Chem. Commun.* **2014**, *50*, 14543-14546.

(27) Aggarwal, H.; Bhatt, P. M.; Bezuidenhout, C. X.; Barbour, L. J. Direct evidence for single-crystal to single-crystal switching of degree of interpenetration in a metal-organic framework. *J. Am. Chem. Soc.* **2014**, *136*, 3776-3779.

(28) Zhang, J.-P.; Lin, Y.-Y.; Zhang, W.-X.; Chen, X.-M. Temperature- or guest-induced drastic single-crystal-to-single-crystal transformations of a nanoporous coordination polymer. *J. Am. Chem. Soc.* **2005**, *127*, 14162-14163.

(29) Reticular Chemistry Structure Resource (RCSR) at http://rcsr.anu.edu.au/.

(30) Hou, L.; Zhang, J.-P.; Chen, X.-M. Two metal-carboxylate frameworks featuring uncommon 2D + 3D and 3-fold-interpenetration: (3,5)-connected isomeric hms and gra Nets. *Cryst. Growth Des.* **2009**, *9*, 2415-2419.

(31) *Materials Studio*, version 4.3; Accelrys: San Diego, CA, 2008.

(32) Gao, C.; Liu, S.; Xie, L.; Ren, Y.; Cao, J.; Sun, C. Design and construction of a microporous

metal-organic framework based on the pillared-layer motif. *CrystEngComm* **2007**, *9*, 545-547.

(33) Jeong, S.; Kim, D.; Song, X.; Choi, M.; Park, N.; Lah, M. S. Postsynthetic exchanges of the pillaring ligand in three-dimensional metal-organic frameworks. *Chem. Mater.* **2013**, *25*, 1047-1054.

(34) Jeong, S.; Kim, D.; Shin, S.; Moon, D.; Cho, S. J.; Lah, M. S. Combinational synthetic approaches for isoreticular and polymorphic metal-organic frameworks with tuned pore geometries and surface properties. *Chem. Mater.* **2014**, *26*, 1711-1719.

(35) Rapid Auto software, R-Axis series, Cat. No. 9220B101, Rigaku Corporation.

(36) Arvai, A. J.; Nielsen, C. ADSC Quantum-210 ADX Program, Area Detector System Corporation; Poway, CA, USA, 1983.

(37) HKL3000 program: Otwinowski Z.; Minor, W. *in Methods in Enzymology*, ed. Carter, Jr. C. W.; Sweet, R. M. Academic Press, New York, 1997, vol. 276, part A, pp. 307.

(38) SHELX program: Sheldrick, G. M. *Acta Crystallogr. Sect. C*, **2015**, 71, 3-8.

(39) PLATON program: Spek, A. L. *Acta Crystallogr. Sect. C*, **2015**, 71, 9-18.

(40) Walton, K. S.; Snurr, R. Q. Applicability of the BET method for determining surface areas of microporous metal-organic frameworks. *J. Am. Chem. Soc.* **2007**, *129*, 8552-8556.

(41) Senkovska, I.; Kaskel, S. Ultrahigh porosity in mesoporous MOFs: promises and limitations. *Chem. Commun.* **2014**, *50*, 7089-7098.

(42) BELMaster Ver. 6.1.0.8, BEL Japan, Inc.

(43) Deria, P.; Mondloch, J. E.; Karagiaridi, O.; Bury, W.; Hupp, J. T.; Farha, O. K. Beyond post-synthesis modification: evolution of metal-organic frameworks via building block replacement. *Chem. Soc. Rev.* **2014**, *43*, 5896-5912.

(44) Burnett, B. J.; Barron, P. M.; Hu, C.; Choe, W. Stepwise synthesis of metal-organic frameworks: replacement of structural organic linkers. *J. Am. Chem. Soc.* **2011**, *133*, 9984-9987.

(45) Kim, M.; Cahill, J. F.; Su, Y.; Prather, A. A.; Cohen, S. M. Postsynthetic ligand exchange as a route to functionalization of 'inert' metal-organic frameworks. *Chem. Sci*. **2012**, *3*, 126-130.

(46) Karagiaridi, O.; Bury, W.; Sarjeant, A. A.; Stern, C. L.; Farha, O. K.; Hupp, J. T. Synthesis and characterization of isostructural cadmium zeolitic imidazolate frameworks via solvent-assisted linker

exchange. *Chem. Sci.* **2012**, *3*, 3256-3260.

II. New Mechanism of Mesopore Generation in Metal-Organic Frameworks

2.1. INTRODUCTION

A single- or mono-crystal is an ideal 'perfect crystal', but all real crystalline materials are mosaic crystals consisting of numerous small perfect crystals (crystallites) randomly misaligned in the reference orientation. The mosaicity represents the degree of misalignment of the crystallites in a crystalline material. Grain boundaries (crystallite boundaries) are interfaces between the crystallites and is generated in the region where the crystallites meet. Grain boundaries have been recognized as important because they greatly affect the mechanical and physical properties of the crystalline materials.[1-3]

Like zeolites, metal-organic frameworks (MOFs) are an extended network and have permanent porosity and topological diversity. To understand crystal growth mechanisms of MOFs, it is important to know zeolite formation hypotheses since the synthetic approaches to zeolites are conceptually similar to those to MOFs (although chemically less diverse than to MOFs).[4] Zeolite crystals have been proposed to grow by attachment of small primary units (monomers or small oligomers) to a crystallite (MONOMER model),[5,6] by attachment of pre-fabricated units similar to structural elements of the final framework (secondary building units (SBUs)) to a crystallite (SBU model),[5,7] or by oriented-aggregation of block-shaped crystallites (NANOSLABs), where the size of the block-shaped crystallites is several nm to several tens of nm (NANOSLAB model).[5,8] Recently, the Dove group has described crystal growth mechanisms as crystallization by particle attachment (CPA), from monomer attachment (the theory of classical crystallization) to the oriented attachment of fully formed nanocrystals.[9]

Studies on the growth mechanism of MOF are limited only in small numbers due to difficulties in TEM analysis in early stage of MOF crystallization because of the instability of MOFs under the electron beam. Patterson et al. reported that the ZIF-8 crystals grew by classical nucleation theory (CNT).[10] On the other hand, Zehng et al. claimed that the MOF-5 crystal grew by NANOSLAB model with 5 nm - 10 nm nanoslab size.[11]

MOFs are interesting porous materials that are composed of metal ions and/or metal clusters that act

as multitopic inorganic nodes with organic ligands acting as linker.[12] The pore geometries and surface properties of the MOFs can be utilized in various applications.[13] However, most of the reported MOFs so far are microporous (pore size < 2 nm), and only a small fraction of MOFs with ordered mesopores (2 – 50 nm) are reported.[14] The small pore size inherently limits the diffusion of larger molecules and their interactions with active sites in MOFs. Researchers are paying attention to produce hierarchically porous MOF (HP-MOF) to overcome the chronic problems of MOFs.

A synthetic strategy for the HP-MOFs is the use of organic linkers and metal-clusters large enough to produce mesopores while their network topologies do not allow interpenetration.[15] Another strategy is the preparation of the MOFs with defects induced by modulators and the subsequent removal of the residuals in the pore or the defect sites by simply washing the MOFs in organic solvents.[16] It is reported that even in-situ etching of the defects generated during the synthesis in extended reaction time by the reaction solvent can lead to an HP-MOF.[17] Various hard and soft templates are employed and subsequently removed for the preparations of HP-MOFs.[18,19] Post-synthetic removal of thermolabile linkers was also utilized for the preparation of HP-MOFs.[20]

Here we present an example of MOF crystal growth by CPA with 5 - 10 nm particle dimensions and also report a new approach for mesopore generation through post-synthetic thermal conversion of a MOF. Recently, we have reported a single-crystal-to-single-crystal (SCSC) transformation of non-interpenetrated MOF [Ni(HBTC)(bipy)] (**1**) with **hms** topology, in which two-dimensional (2-D) sheets made of Ni(II) ion and 1,3,5-benzene tricarboxylates ($HBTC^{2-}$/BTC^{3-}) are connected to each other via 4,4′-bipyridine (bipy) pillars, to a doubly-interpenetrated MOF with **hms-c** topology by heating (Fig. 1).[21]

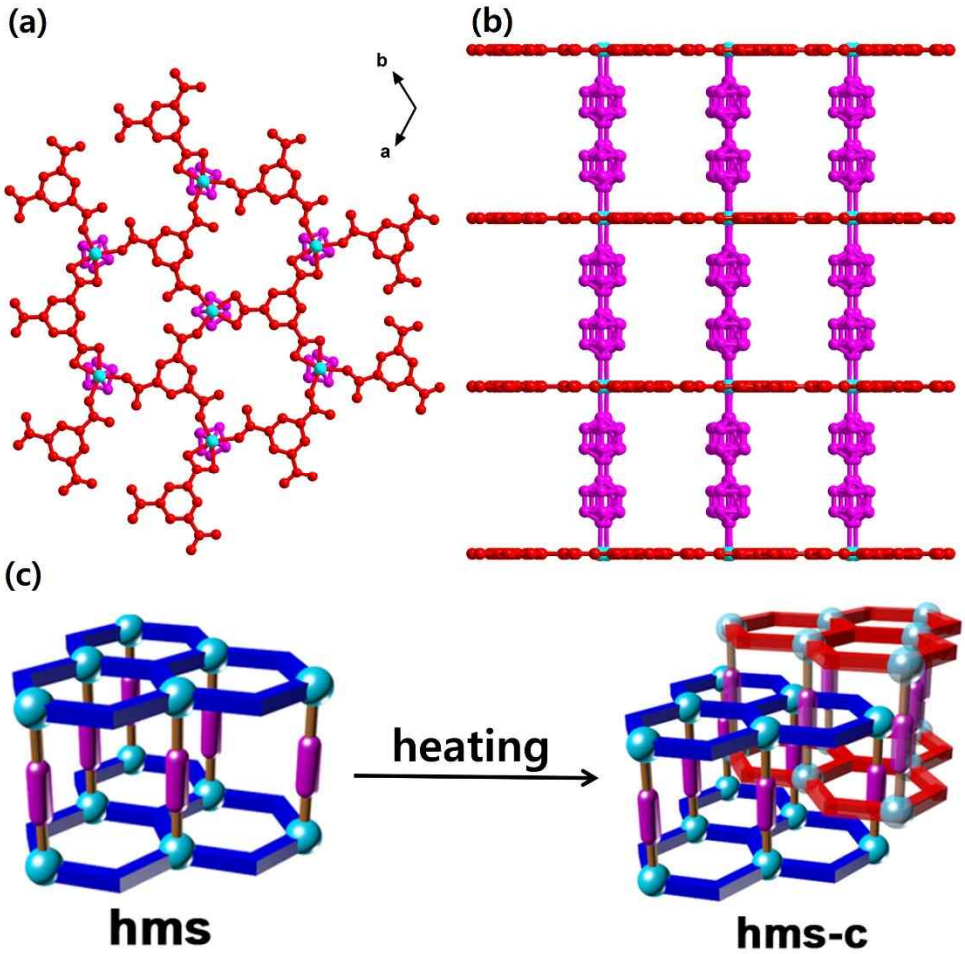

Figure 2.1. (a) Top and (b) side views of the ball-and-stick diagrams of **1.** (c) Conversion of non-interpenetrated hms topology to doubly interpenetrated hms-c topology.

The SCSC transformation from non-interpenetrated **1** to 2-fold interpenetrated **1** must accompany the contraction of the total crystal volume during the conversion since the interpenetration increases the crystal density. All the crystallites in the highly mosaic crystal of **1** are contracted during the thermal conversion. The aggregations of the contracted crystallites are throughout the whole single crystal but localized and limited only up to ~ 100 crystallites, which leads to the generation of mesopores between localized crystallite aggregates (hereafter a non-aggregated single crystallite or the aggregate of several crystallites is called as a grain or a domain) (Scheme 2.1).

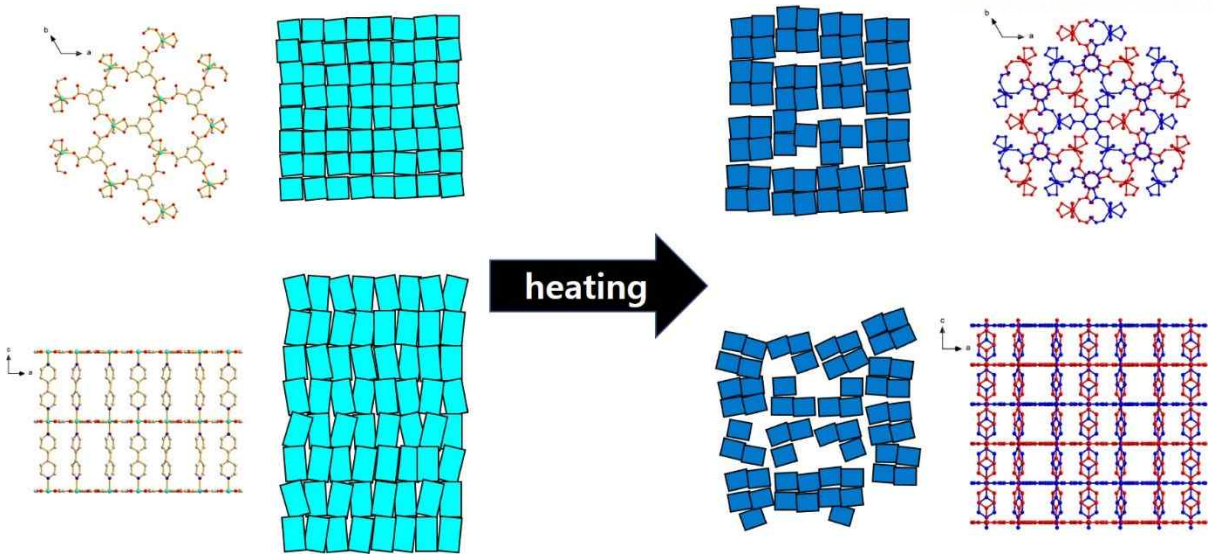

Scheme 2.1. Mesopore generation by thermal conversions.

2.2. Experimental section

General Procedures

All reagents were purchased from commercial sources and used without further purification. 1H nuclear magnetic resonance (NMR) spectra were recorded using a VNMRS 600 MHz FT-NMR spectrophotometer. Powder X-ray diffraction (PXRD) data were recorded using a Bruker D2 Phaser automated diffractometer at room temperature with a step size of 0.02° in 2θ angle. Simulated PXRD patterns were calculated with Materials Studio software[S1] using single-crystal data. All gas sorption isotherms were measured using a BELSORP-max (BEL Japan, Inc.) with a standard volumetric technique using N2 (with purity of 99.999%) as an adsorbate.

Synthesis of structure

Preparation of non-interpenetrated **[Ni(HBTC)(bipy)]-hms**, **1**. **1** with hms topology was prepared according to the reported procedure.[S2] Activated **1** was prepared by vacuuming (~10−2 torr) the as-synthesized sample pre-soaked in methylene chloride (MC) at ambient temperature for 1 d.

Preparation of hierarchically porous **[Ni(HBTC)(bipy)]**, **1(T,t)**, (where **T** and **t** are aging temperature in Celsius and aging time in hour, respectively). An approximate 40 mg amount of as-synthesized non-interpenetrated **1** with hms topology pre-washed using fresh DMF were air-dried at ambient condition for 3 h. The sample was heated up to 200 °C, 250 °C, 275 °C, 300 °C and 350 °C under flowing nitrogen gas with a heating rate of 10 °C min^{-1} and aged for 0, 0.25, 0.5, 1, 5, 12 h and 24 h respectively, and then slowly cooled to ambient temperature (22-23 °C) under flowing N_2. Activated samples were prepared by vacuuming (~10−2 torr) the corresponding non-activated samples at 150 °C for 3 h.

2.3. RESULTS AND DISCUSSION

Optical micrographs of air-dried **1** show a transparent single crystal with a hexagonal block that is split in half (Figure 2.2). However, the SEM images of a single crystal indicate that it is an assembly of numerous crystallites of 5 nm to 6 nm dimensions (Figure 2.3). In addition, the crystal has numerous cracks with 100-200 nm width all over the surface. The crystallites are observed not only at the surface but also at the inside of the crystal. SEM images of the fragmented **1** obtained by mechanical grinding also showed numerous crystallite at the inside of the crystal (Figure 2.5). The SEM observation of **1** indicated that the single crystal of **1** was not obtained by CNT but by CPA with 5 - 6 nm particle dimensions.

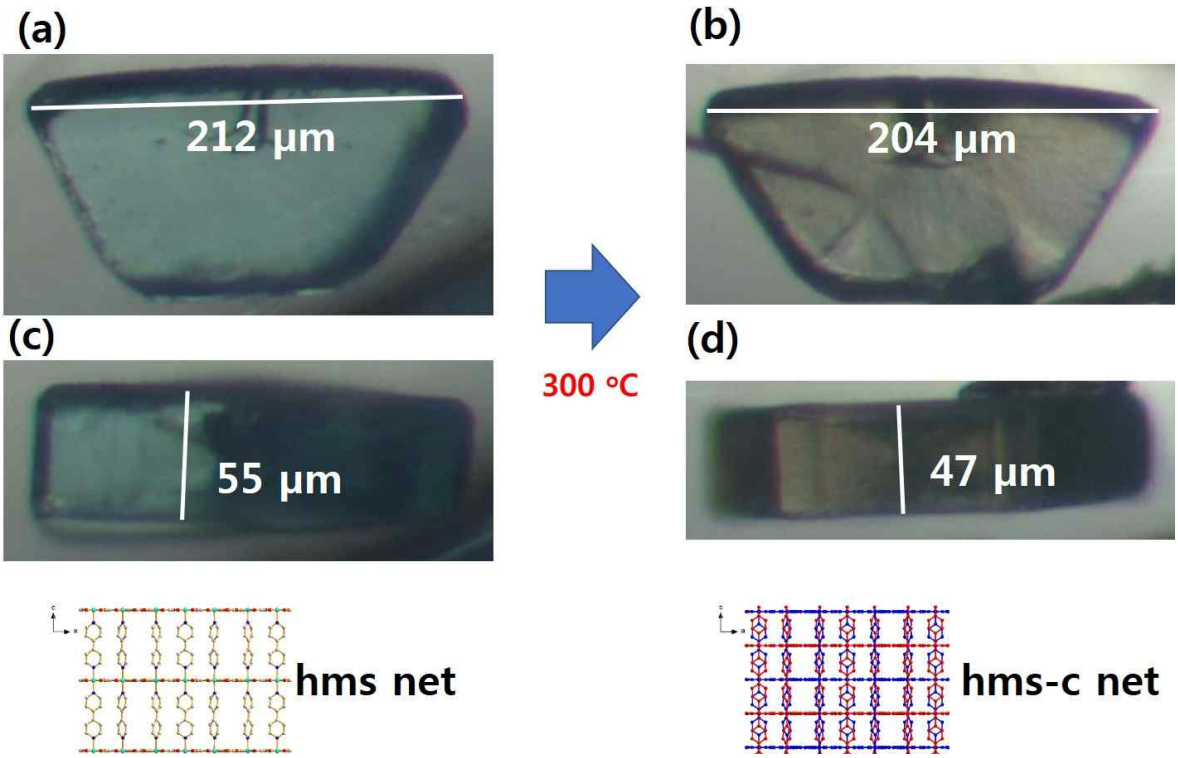

Figure 2.2. Optical photographs of **1** and **1(300, 1)**.

When air-dried **1** was aged at 200 °C under N_2 for 1 h, all the cracks at the surface of the single crystal disappeared and the size of the domains slightly increased even though the transformation of the non-interpenetrated structure to the partially interpenetrated structure must lead to the contraction of a single crystallite dimension (Fig. 2b). The increase of domain dimension is not due to the increase of a single crystallite size but due to the aggregation of several crystallites. Several small crystallites aggregate to form a domain with ~10 nm dimension. When aged at 250 °C, the size of the domain increased to 10 - 20 nm and the generation of meso pores between the domains with 15 nm dimension were observed (Figure 2.3). In the side view, long cracks are formed (Figure 2.4). These cracks are thought to be a kind of grain boundary that appears partly because the orientation of the domains is different from that of neighboring domains as the domains undergo conversion and oligomerization. The PXRD patterns of **1** aged at 200 °C and 250 °C, respectively, show that non-interpenetrated domains still exist even if the aging time is increased (Figure 2.6). When aged at 275 °C, the MOFs at all the domains are completely interpenetrated (Figure 2.7). At this temperature, the grain boundaries have increased

considerably because the orientation of the newly formed domains has changed in many areas (Figure 2.4). When the temperature is 300 ° C, the domains become more oligomerized and oriented attachment occurs between the domains, resulting in a larger meso pore size (Scheme 2.2).

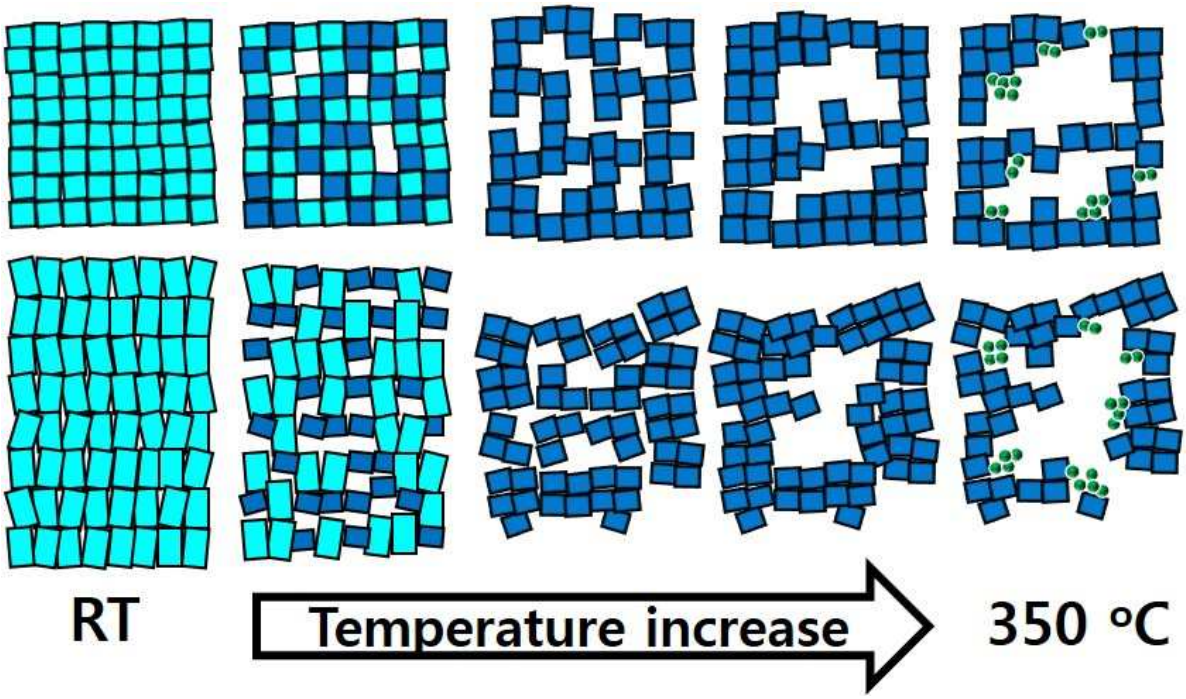

Scheme 2.2. Thermal conversions from non-interpenetrated microporous MOFs to hierarchically porous MOFs.

In the side view of the SEM image, the grain boundaries at 275 °C were significantly reduced at 300 °C (Figure 2.4). At first, the domain volume is reduced to half by interpenetration of domains, while the volume of the entire crystal is not big changed, so meso size spaces are created inside the crystal. Then, domains with partially misaligned orientations are re-orientated and domains become more clustered, resulting in a larger meso pore size. Firstly, as the temperature increases, the pore changes by the combination of the conversion of non-interpenetrated domain to interpenetrated domain and the boundary change between the domains. However, when the temperature reaches a certain temperature, the domain conversion stops and the pore shape changes only due to the boundary change between the domains (Scheme 2.2). If the non-interpenetrated **1** is changed to double interpenetrate, the length of the c-axis shall be reduced by half. However, compared with the optical photograph of **1** and **1(300, 1)**,

there is little change in length to the a-b plane, and only 15% decrease in length to the c-axis (Figure 2.2). When the temperature is further increased to 350 ℃, a part of the domain is decomposed and Ni nanoparticles are generated (Figure 2.8 & 2.16). As a result, the meso pore size becomes larger and a new boundary in the a-b plane direction is generated (Figure 2.4). These boundaries are gaps created by the oligomerization of domains and the conversion of a portion of the domain into a Ni nanoparticle.

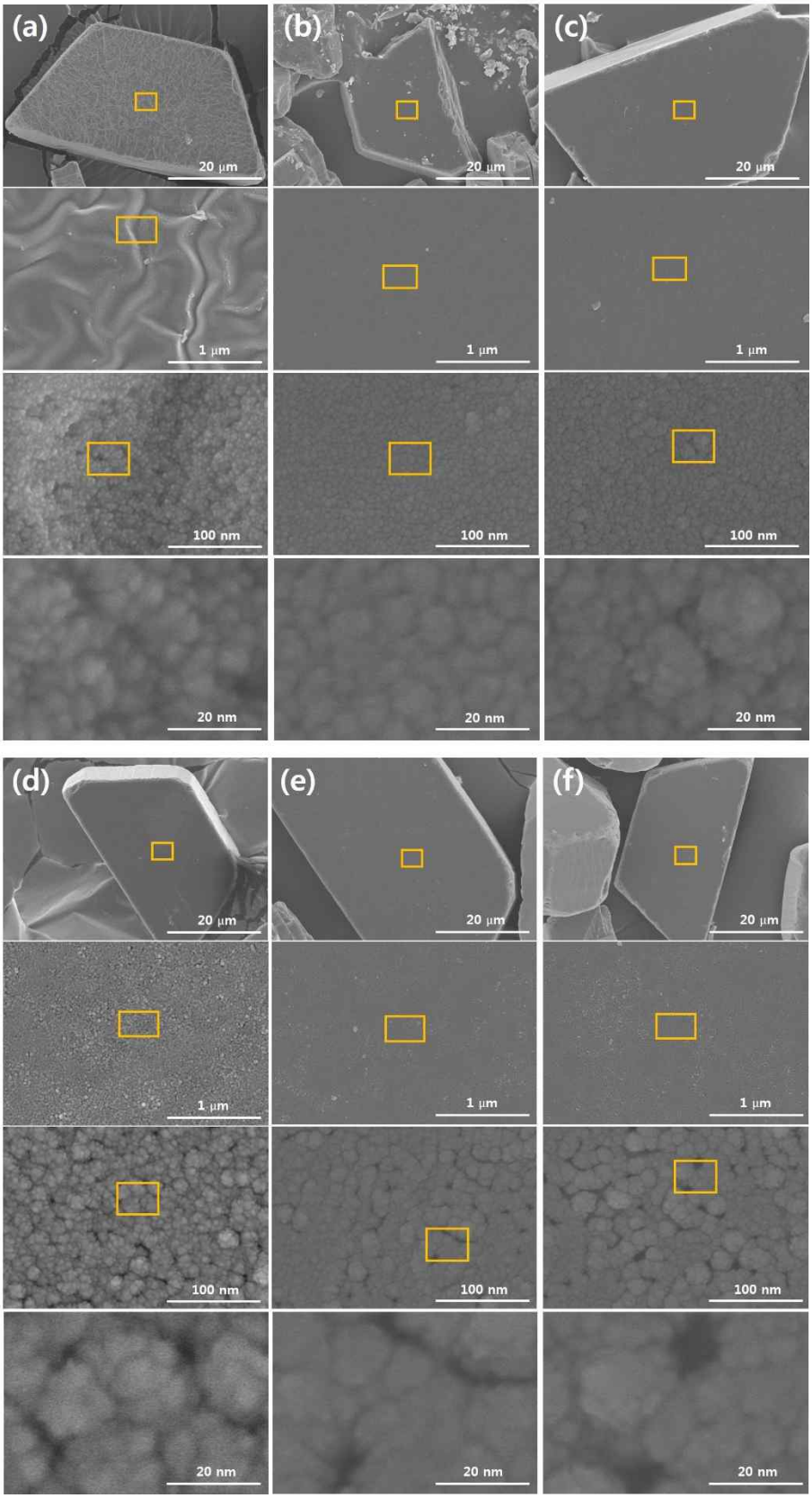

Figure 2.3. SEM images of **1. 1(200, 1), 1(250, 1), 1(275, 1), 1(300, 1)** and **1(350, 1)** top view.

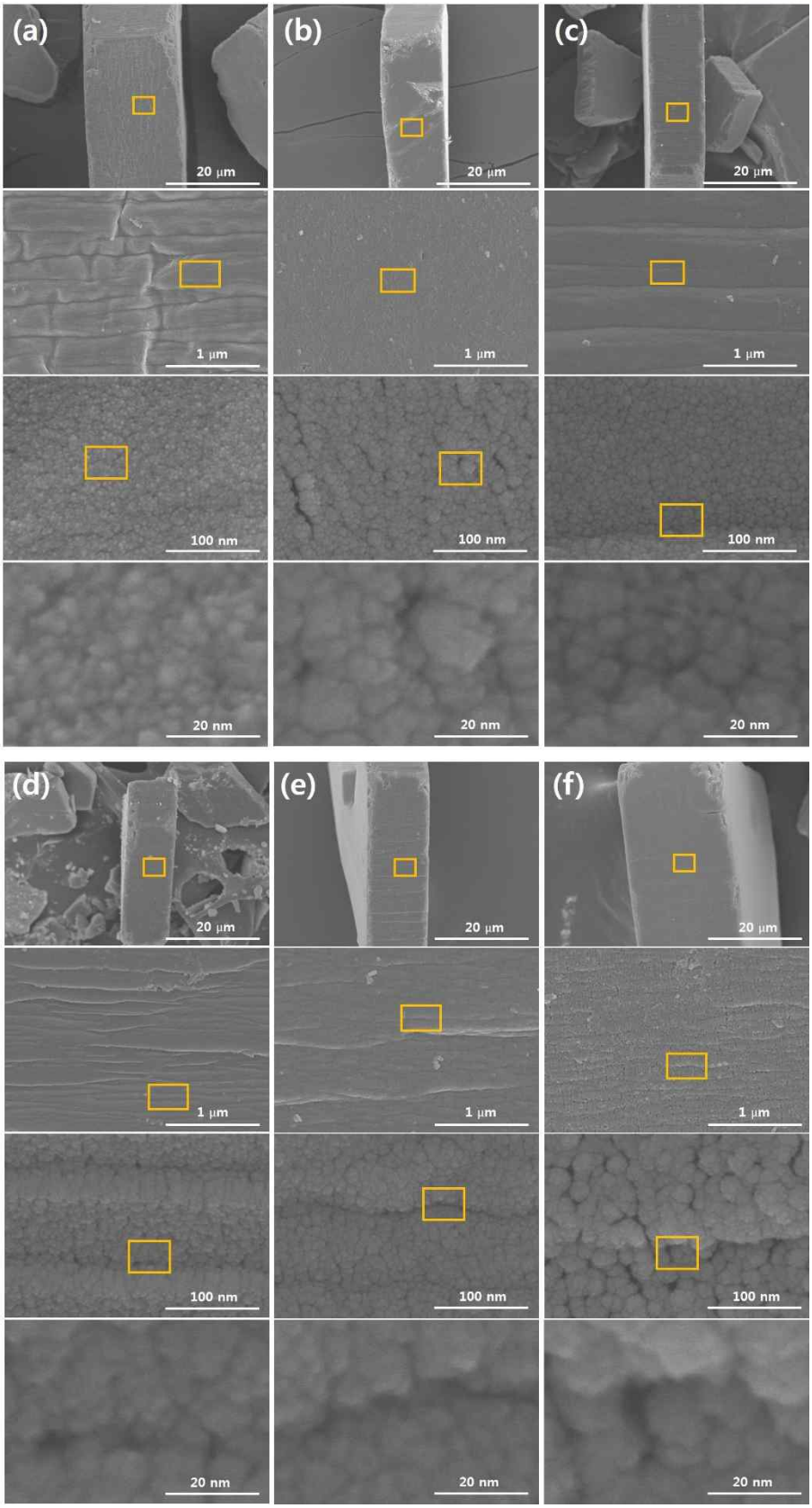

Figure 2.4. SEM images of **1, 1(200, 1), 1(250, 1), 1(275, 1), 1(300, 1)** and **1(350, 1)** side view.

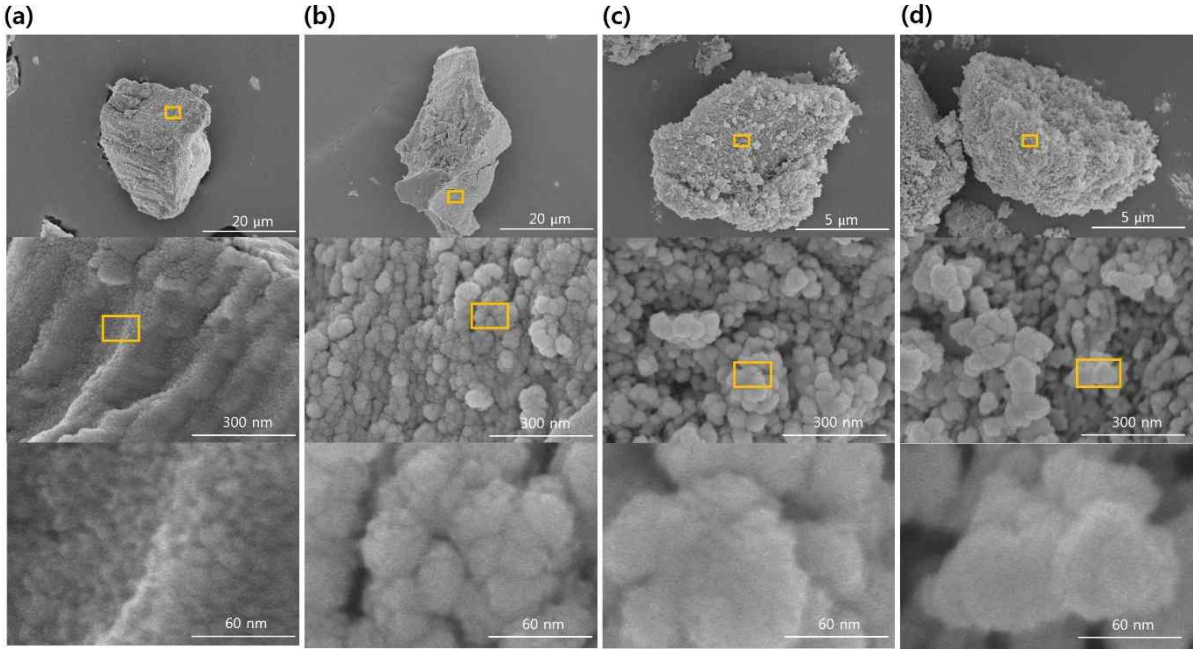

Figure 2.5. SEM images of grinded (a) **1** (b) **1(200, 1)** (c) **1(300, 1)** (d) **1(350, 1)**

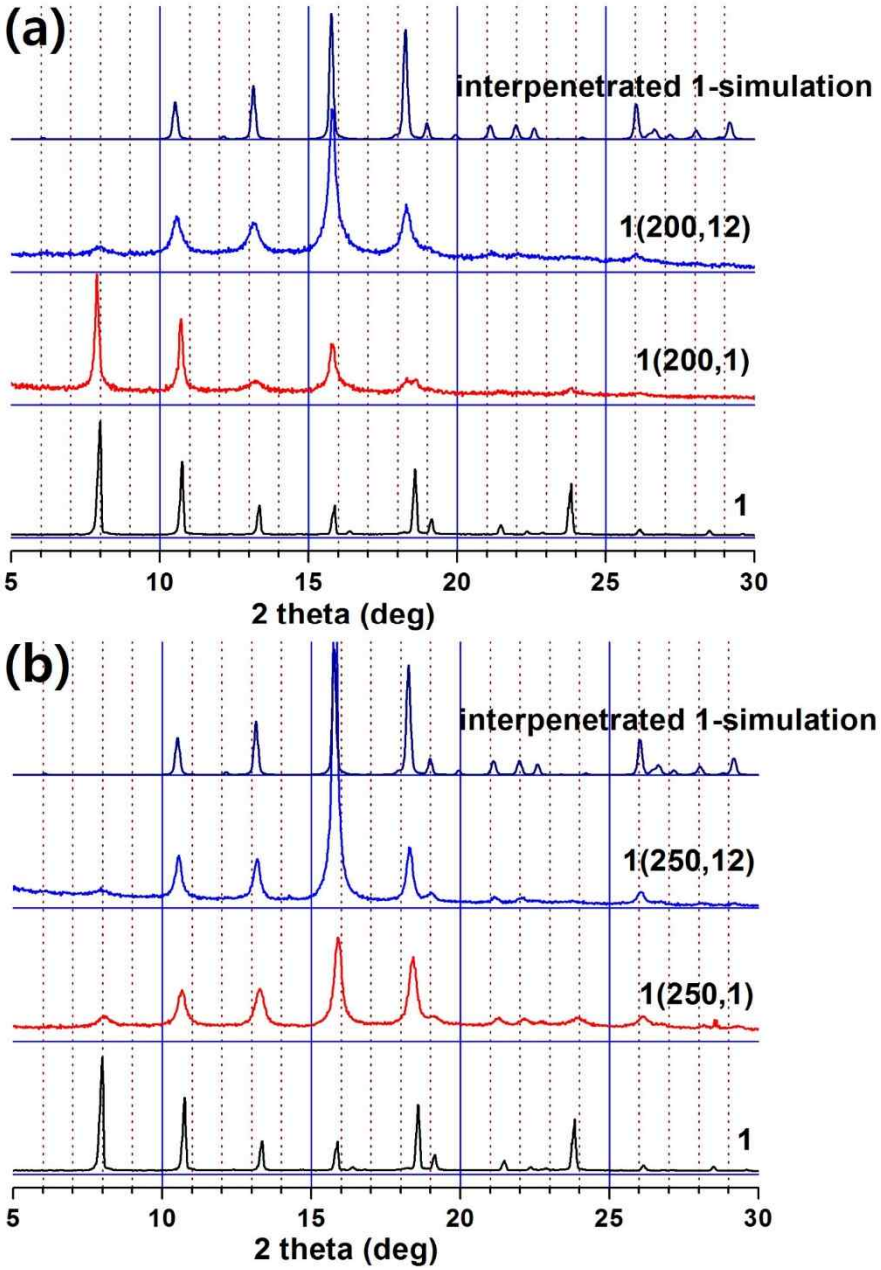

Figure 2.6. The PXRD patterns of **(a) 1(200,t)** and **(b) 1(250,t)**.

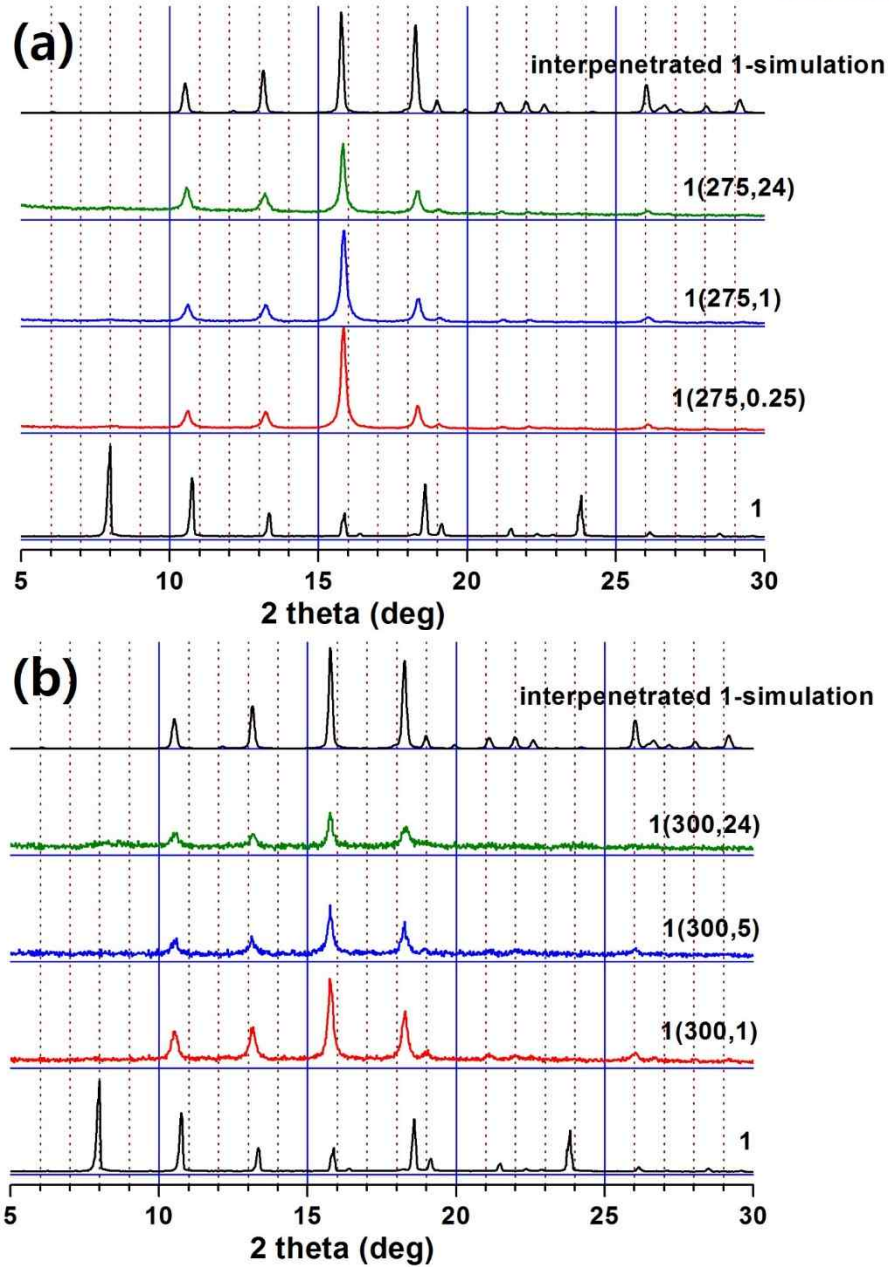

Figure 2.7. The PXRD patterns of (a) **1(275,t)** and (b) **1(300,t)**.

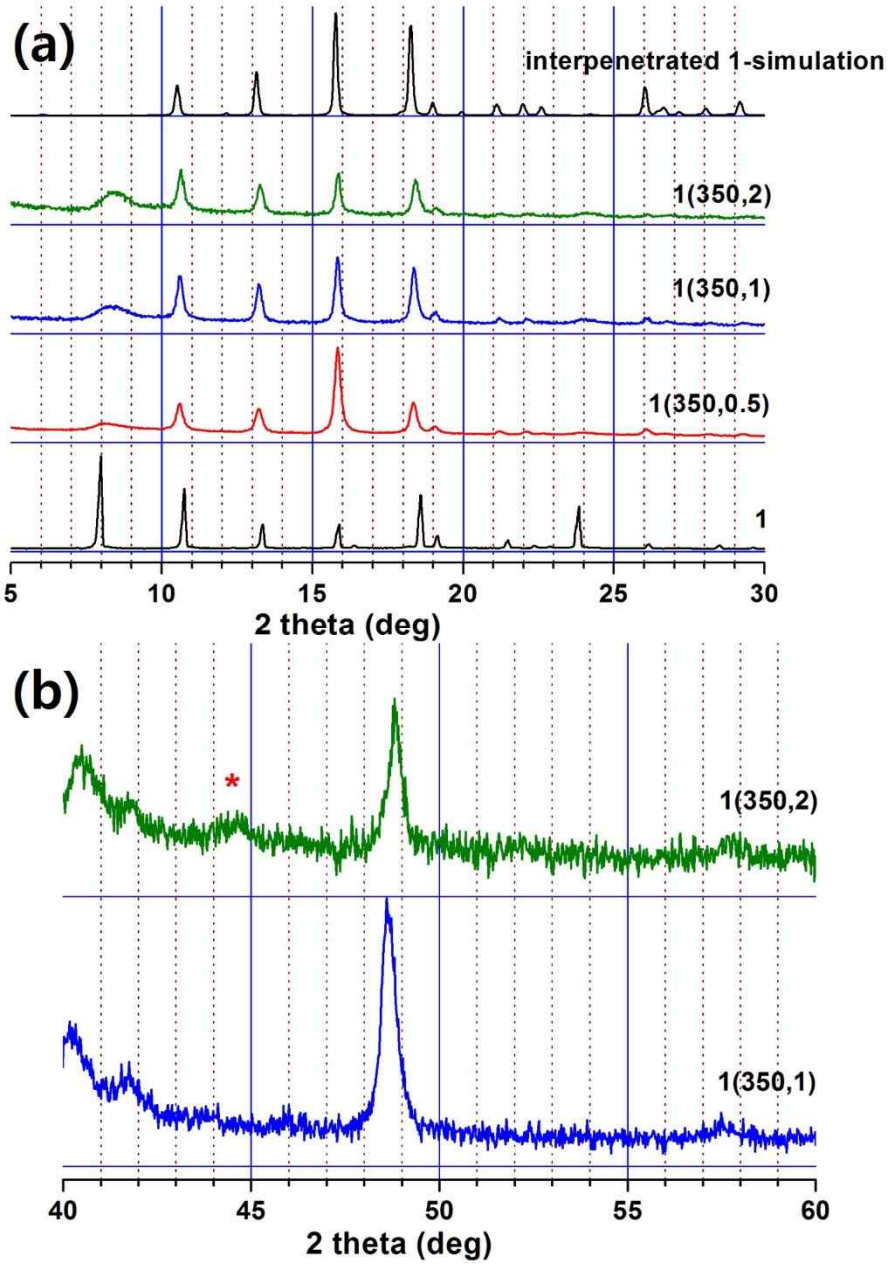

Figure 2.8. The PXRD patterns of (a) **1(350,t)** and (b) **1(350,1)** and **1(350,2)** with 2 theta range of 40-60 degree (* is peak of Ni nanoparticles).

N_2 sorption at 77 K and pore size distribution show that **1** is a microporous material while **1(200, t)** is a hierarchically porous MOF with both micro and meso pores simultaneously (Figure 2.9). As the aging time increases, the amount of micropore decreases and the amount of meso pore increases (Figure 2.10). This is because the domains are interpenetrating and the micro pores of the domains are reduced, while the meso pores are increasing because of the boundary between the domains. In the pore size distribution, as the aging time increases, the size of the meso pore increases, and the PXRD pattern shows that **1** is converted to **interpenetrated 1** (Figure 2.6). However, even with sufficient time, a peak of **1** in PXRD remains, indicating that perfect conversion does not occur at this temperature. **1(250, t)** is also HP-MOF with micro and meso pores. Since the conversion of the domain has already proceeded considerably, the micro pore change due to aging time is small, but the meso pore change due to the boundary between the domains is large. As shown in the pore size distribution, it can be seen that the meso pore size of **1(250, t)** varies from 10 nm to 20 nm (Figure 2.11). **1(275, t)** is the state that conversion of all domains is completed. The N_2 sorption at 77 K shows no change in micropores with aging time, but only meso pore changes. In the pore size distribution analysis, the size of the meso pore varies with aging time, but the micro pore does not change (Figure 2.12). After the reduction of the micropores due to the conversion of the domains, there is no change in the domains and only the meso pores are changed because the pore changes only by the boundary between the domains. The reason why the domain is selectively changed at a certain temperature is considered to be that the domain is converted from a small domain having a relatively low energy to be converted. **1(300, t)** is very similar to **1(275, t)** considering that meso pore increases with increasing aging time. The difference is that **1(300, t)** shows decrease in micropore when aging time is increased up to 24 hours (Figure 2.13). The reason for the decrease in micropores is that there is no change in the domain from 300 °C until a certain aging time, but after a certain period of time, crystals collapse and Ni nanoparticles are formed. Since the amount is too little and size is small, the peak of Ni nanoparticle is not observed in PXRD, but it can be confirmed through HR TEM image (Figure 2.14). In **1(350, t)**, micro pore was significantly decreased, and pore size increased meso pore to macro pore according to aging time (Figure 2.15). At this temperature, PXRD and HR TEM images show that a crystal collapses and Ni nanoparticles are formed

(Figure 2.8 & 2.16).

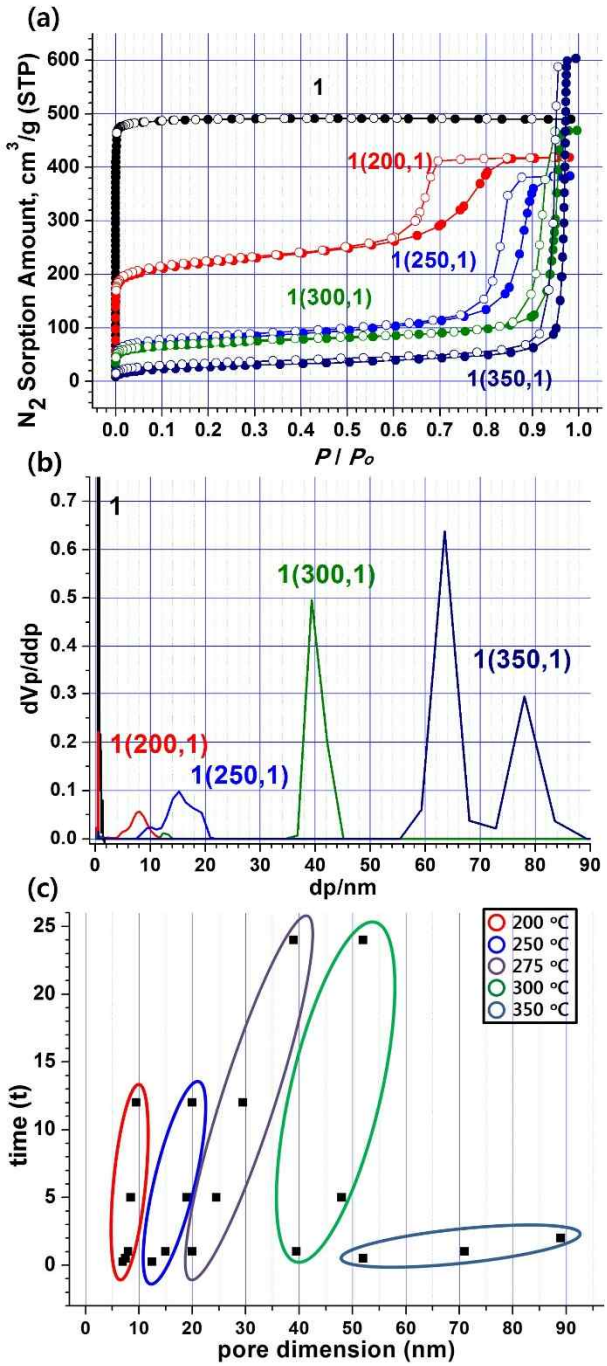

Figure 2.9. (a) The N_2 sorption isotherms of **1(T, 1)** at 77 K and (b) the pore size distributions. (c) The pore size distributions of **1(T, t)** depending on aging time and temperature.

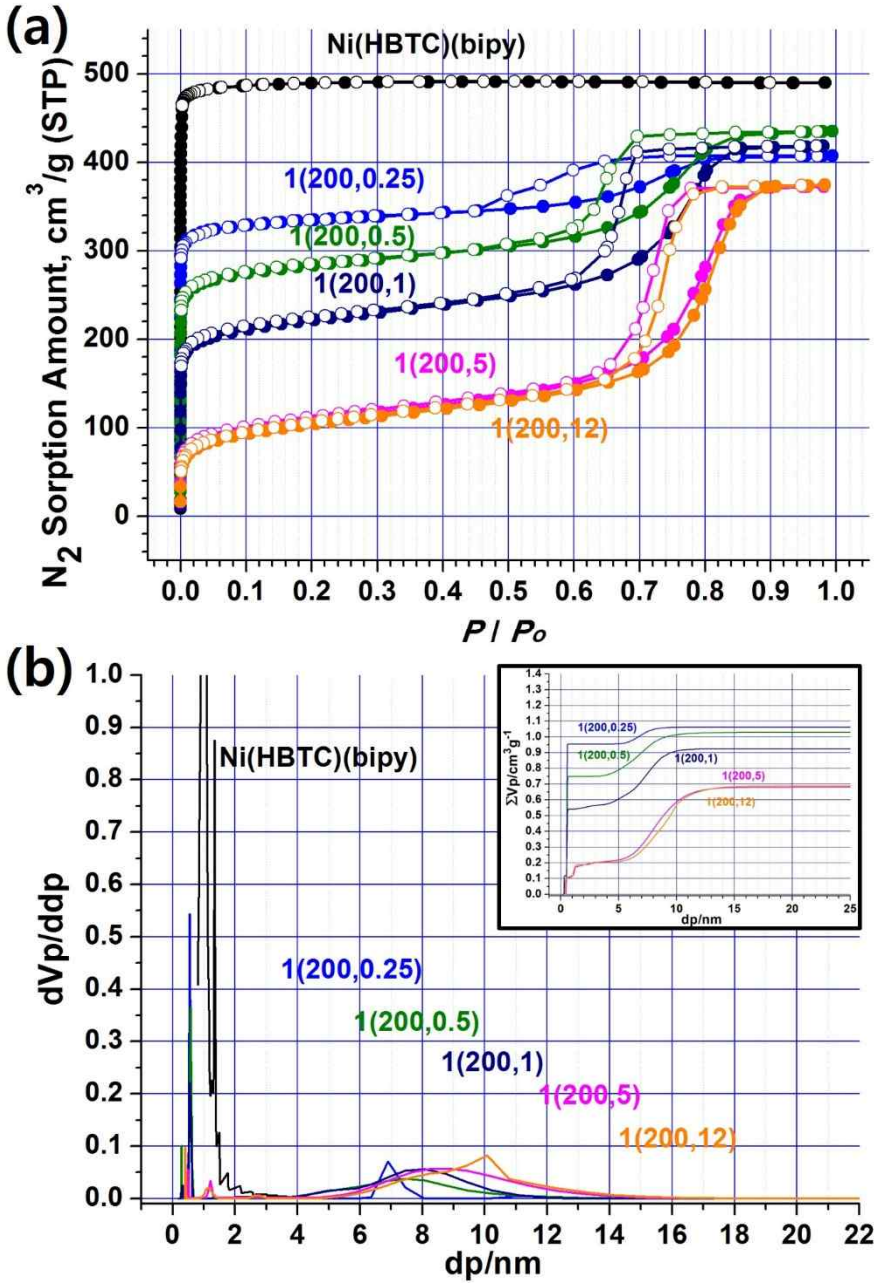

Figure 2.10. The N_2 sorption isotherms of (a) **1(200, t)** at 77 K. Adsorption and desorption isotherms are represented by filled and empty circles, respectively. (b) The pore size distributions and cumulative in the box of **1(200, t)**

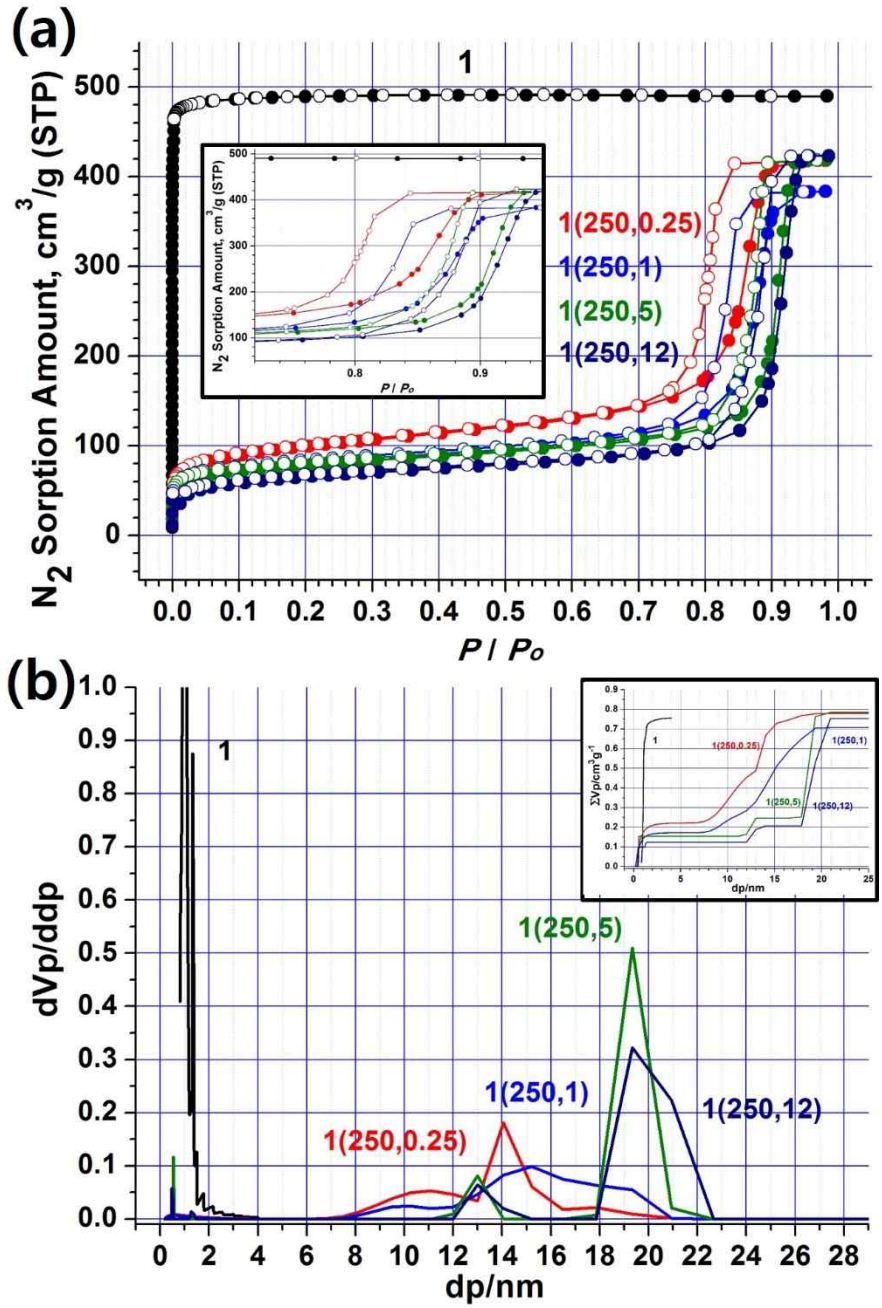

Figure 2.11. The N_2 sorption isotherms of (a) **1(250, t)** at 77 K. Adsorption and desorption isotherms are represented by filled and empty circles, respectively. (b) The pore size distributions and cumulative in the box of **1(250, t)**

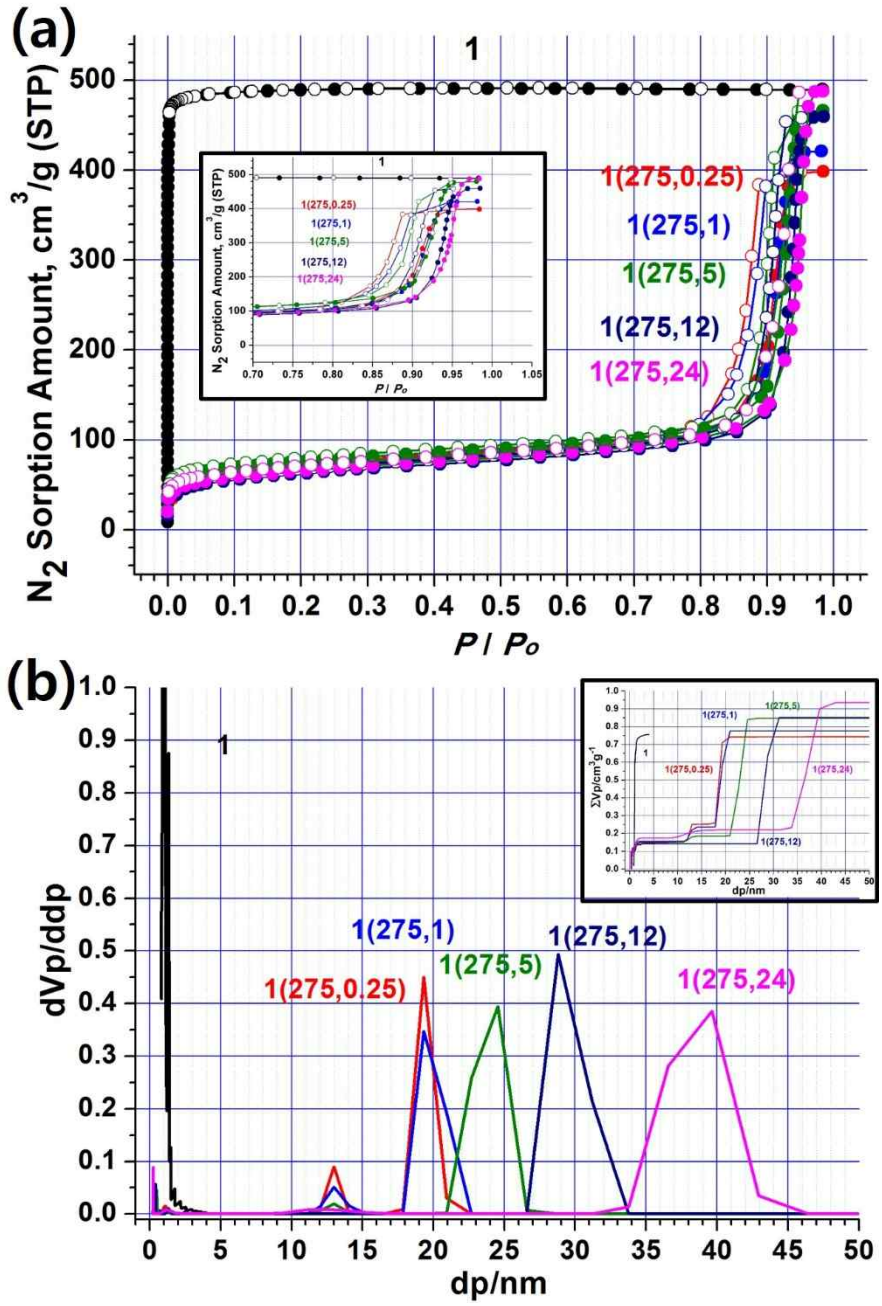

Figure 2.12. The N_2 sorption isotherms of (a) **1(275, t)** at 77 K. Adsorption and desorption isotherms are represented by filled and empty circles, respectively. (b) The pore size distributions and cumulative in the box of **1(275, t)**

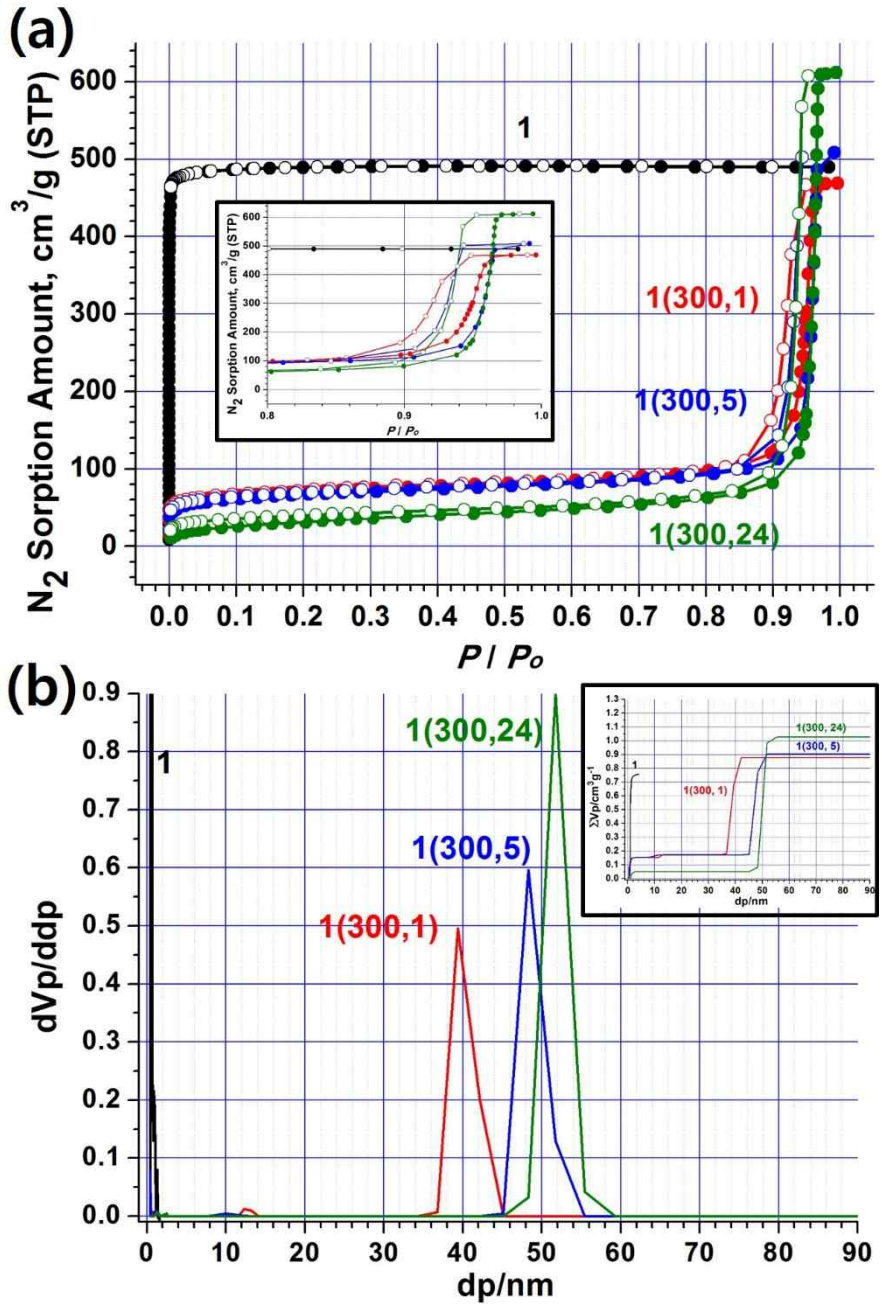

Figure 2.13. The N_2 sorption isotherms of (a) **1(300, t)** at 77 K. Adsorption and desorption isotherms are represented by filled and empty circles, respectively. (b) The pore size distributions and cumulative in the box of **1(300, t)**

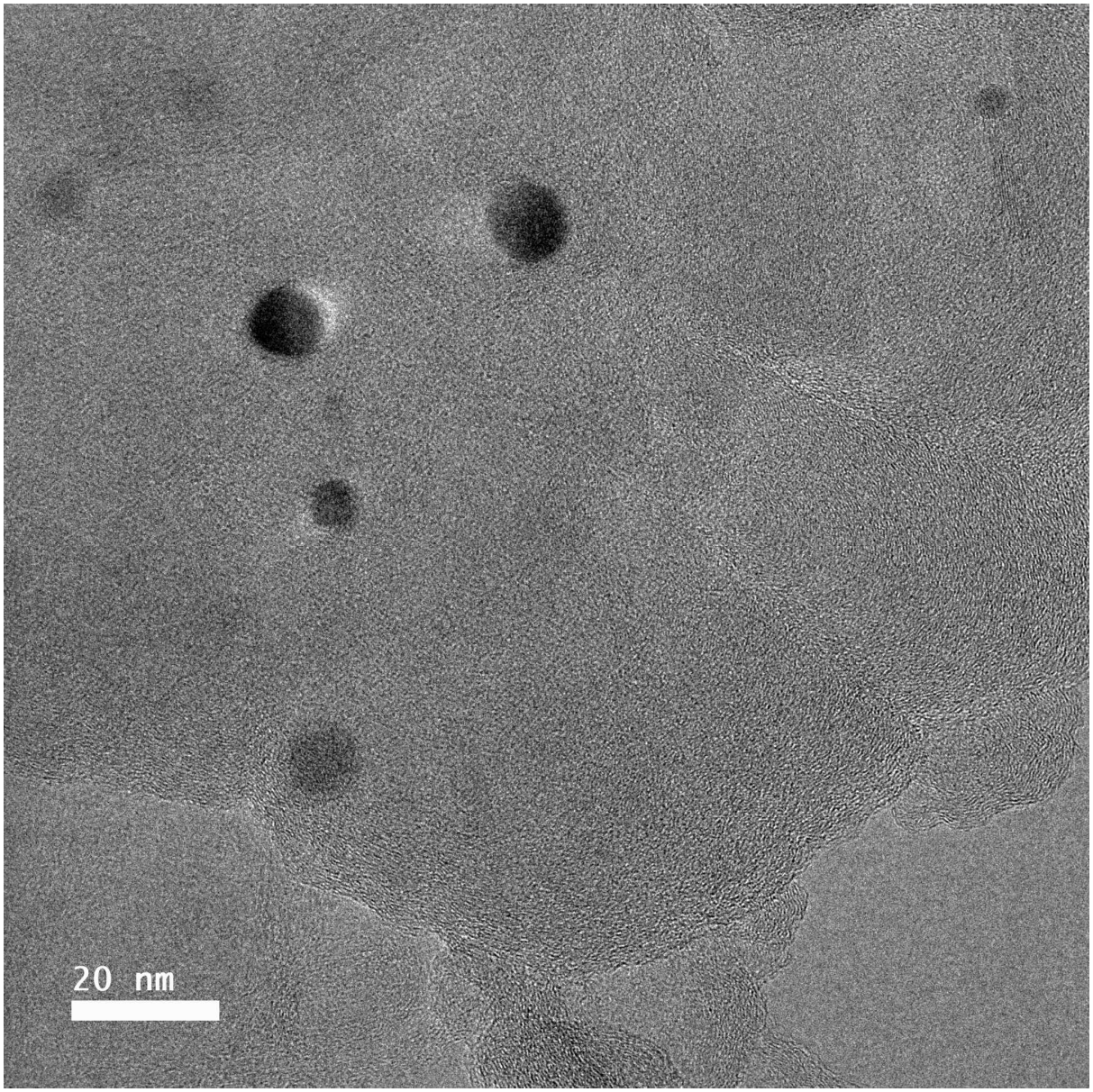

Figure 2.14. HR TEM images of **1(300, 24)**.

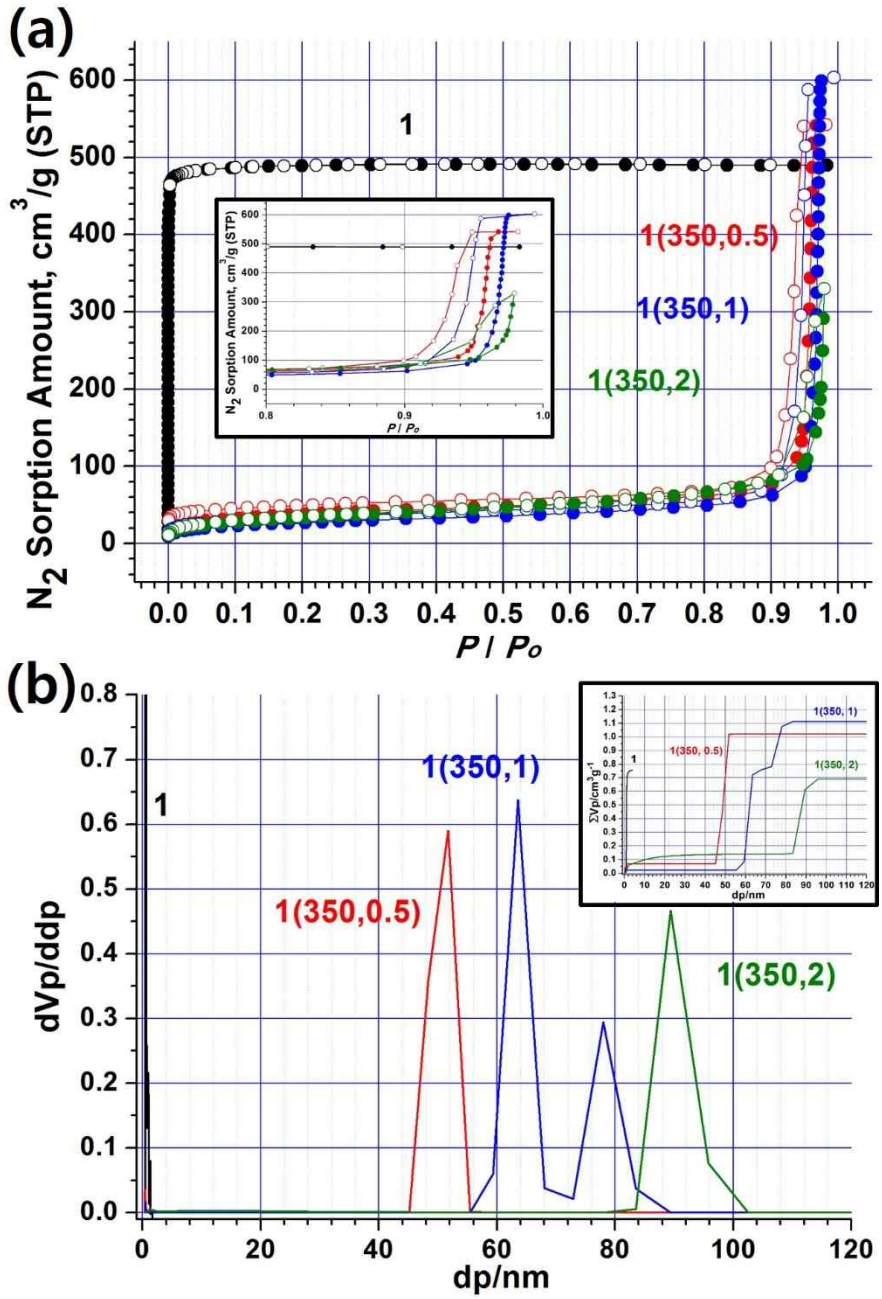

Figure 2.15. The N_2 sorption isotherms of (a) **1(350, t)** at 77 K. Adsorption and desorption isotherms are represented by filled and empty circles, respectively. (b) The pore size distributions and cumulative in the box of **1(350, t)**

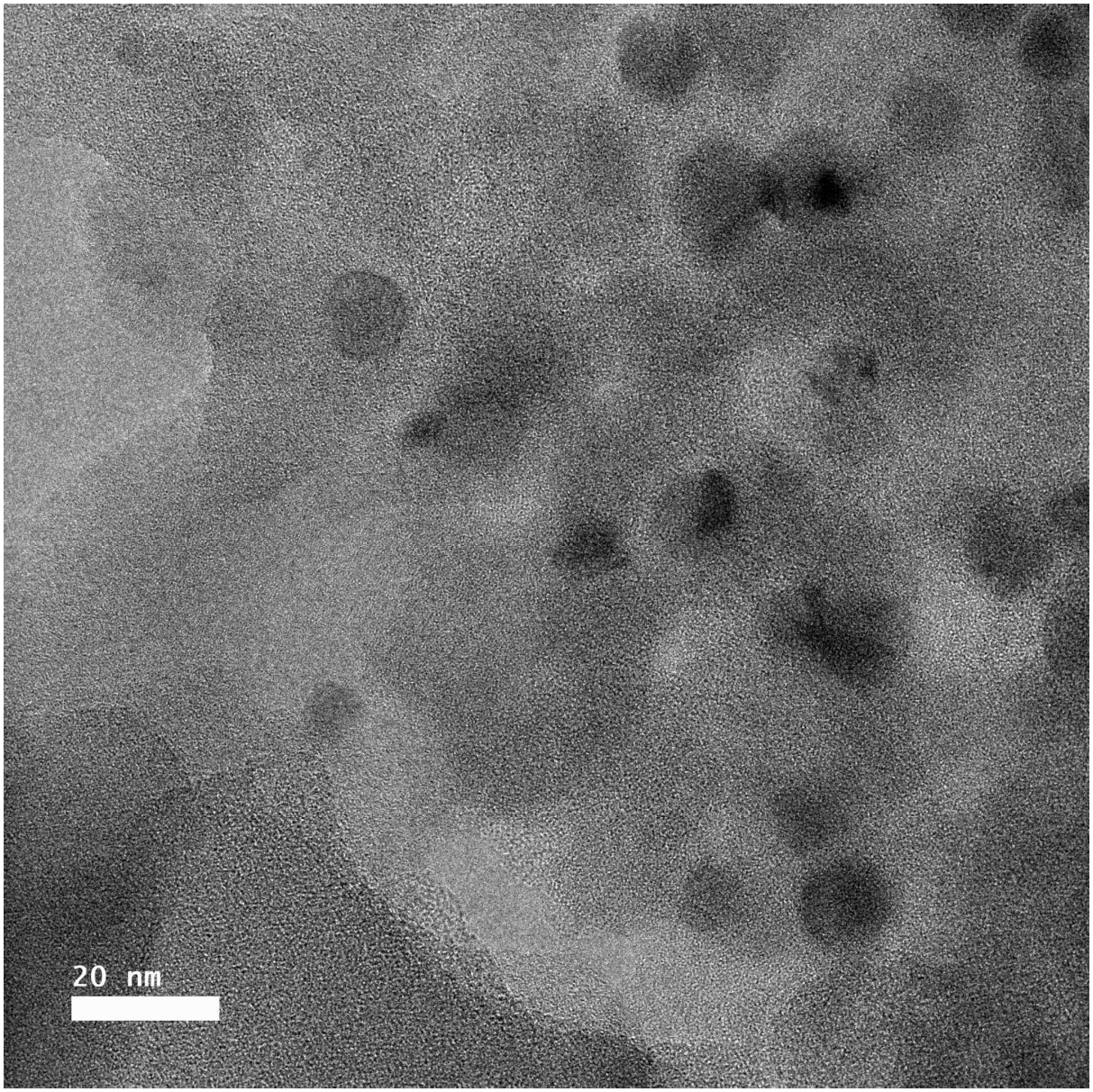

Figure 2.16. HR TEM images of **1(350, 1)**.

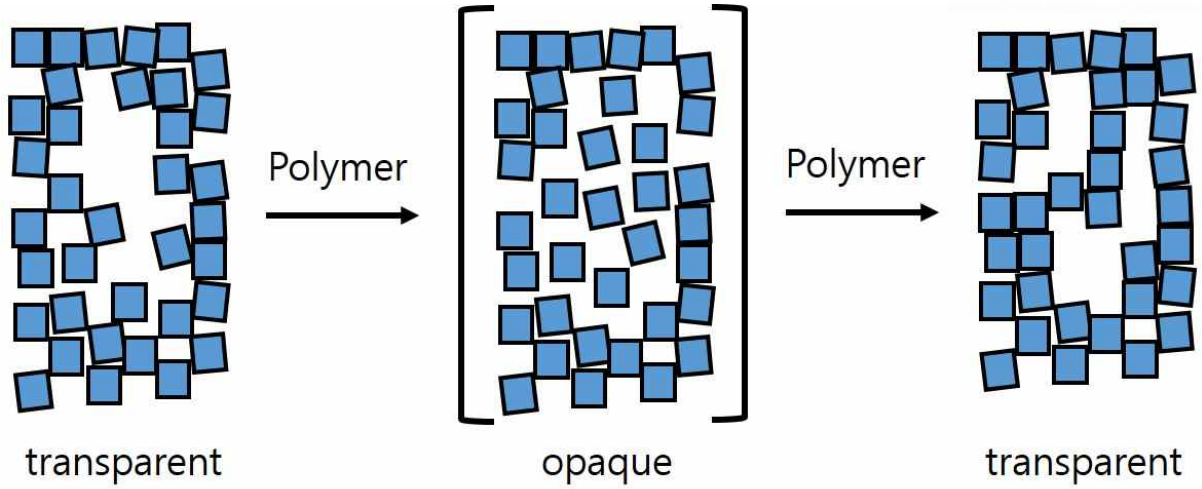

Scheme 2.3. Prediction scheme of rearrangement by polymer in HP-MOF

An interesting phenomenon occurs when the polymer is added to HP-MOF **1(T, t)** with T ≥ 200 °C. When **1(275, 1)** is taken into Paraton oil, the transparent crystal becomes opaque, and then turns back to transparent within a couple of minutes (Figure 2.17). The connection between the domains attached via weak interactions is broken by the introduction of Paraton oil, rearrangement of the domains takes place, and then the orientated attachment of the domains occurs (Scheme 2.3). This phenomenon does not occur in ordinary organic solvents (for examples, *N*,*N*-dimethylformamide, methylene chloride, etc.) and occurs only in polymeric solutions. The polymers that enter the mesopores of crystal. **1(275, 1)** result in oriented rearrangement of the domains. From the point of view of X-ray diffraction, even if the domains are scattered in the polymer, the number is small, and if the ordering is not largely deviated, the diffraction pattern is not greatly affected. In practice, when we analyse the structure of single crystal X-ray diffraction data in three different rearrangement stages (before the rearrangement stage, during the rearrangement stage, after the rearrangement stage) using one single crystal, the structural differences between the stages are minimal (Table 2.1). On the other hand, light scattering behaviour of the three different stages are completely different; a transparent single crystal in polymeric solution under optical light illumination becomes to opaque within ~ 45 seconds, and then turns back to transparent within 2 minutes.

Table 2.1. Single crystal X-ray data of **1(275, 1)** at 173 K.

sample	before putting the polymer	opaque state	again transparent state
space group	*C*2	*C*2	*C*2
reflns_#_tot	16124	16264	15741
reflns_#_gt	7983	7656	5878
R(full)	0.1596	0.1644	0.1710
R(>2s)	0.1089	0.1049	0.0891
wR2(full)	0.2977	0.2924	0.2687
wR2(>2s)	0.2497	0.2437	0.2163
GOF	0.96	0.92	0.86

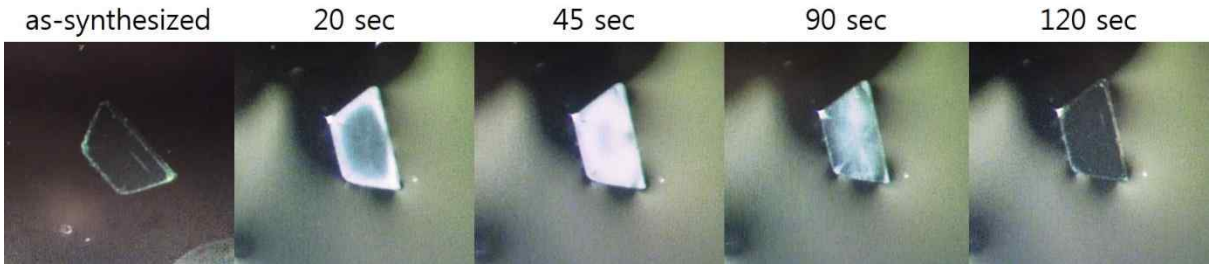

Figure 2.17. Optical photographs of **1(275, 1)** after soaking Paraton oil.

Figure 2.18. Optical photographs of the activated crystals of **1**, **1(200, 5)**, **1(250,12), 1(300,1)** and **1(350,2)**.

Table 2.2. Pore properties of **1** and **1(T,t)**.

MOFs	N_2 uptake 77 K, 1 bar (cm^3/g)	BET surface area[a] (m^2/g)	$V_{p,\ measured}$[b] (cm^3/g)	meso or macro pore dimension[c] (nm)	V(meso and macro)[d]/ V(micro)[e]
1	490	1940	0.76	-	0
1(200,0.25)	408	1340	0.63	7	0.15/0.48(0.31)
1(200,0.5)	435	1100	0.67	7.5	0.30/0.37(0.81)
1(200,1)	418	830	0.65	8.0	0.39/0.26(1.50)
1(200,5)	373	370	0.58	8.5	0.50/0.08(6.25)
1(200,12)	374	370	0.58	9.5	0.51/0.07(7.29)
1(250, 0.25)	418	350	0.65	11, 14	0.56/0.09(6.22)
1(250, 1)	384	280	0.59	15	0.53/0.06(8.83)
1(250, 5)	419	280	0.65	19	0.57/0.08(7.13)
1(250, 12)	423	240	0.65	20	0.60/0.05(12.00)
1(275, 1)	421	250	0.65	20	0.58/0.07(8.29)
1(275, 5)	466	270	0.72	24.5	065/0.07(9.29)
1(275, 12)	460	230	0.71	29.5	0.65/0.06(10.83)
1(275, 24)	488	230	0.76	39	0.69/0.07(9.86)
1(300, 1)	469	260	0.72	39.5	0.65/0.07(9.29)
1(300, 5)	509	240	0.79	48	0.71/0.08(8.88)
1(300, 24)	612	120	0.95	52	0.93/0.02(46.50)
1(350, 0.5)	542	130	0.84	52	0.81/0.03(27.00)
1(350, 1)	603	100	0.93	64, 78	0.91/0.02(45.50)
1(350, 2)	330	120	0.51	89	0.34/0.17(2)

[a]Brunauer-Emmett-Teller surface area. [b]Total pore volume determined by using the adsorption branch of the N_2 isotherm at P/P0 = 0.95. [c]Meso- or macropore dimension determined by the density functional theory method in the adsorption branch of the N_2 isotherm at 77 K. [d]Specific mesopore or macropore volume obtained from the BJH cumulative specific adsorption volume of pores of 1.70−300.00 nm in diameter. [e]Specific micropore volume calculated by subtracting V_{meso} from V_p.

2.4. CONCLUSIONS

Growth mechanism of **1** does not support the classical nucleation process (CNT) and is thought to be made up of a number of domains of 5-10 nm in size. On the other hand, it is already known that **1** is converted to interpenetrated material by increasing the temperature through PSM. A new approach for mesopore generation is demonstrated using the MOF crystals of **1** consisting of numerous domains. When the temperature is raised, each domain is interpenetrated and the volume is reduced by half. However, since the entire crystal volume is not reduced by half during conversion, a mesopore is formed inside the crystal. Also, by varying the temperature and aging time, the size of the mesopore can be carefully controlled.

2.5. REFERENCES

1. Zhu, X., Zhang, G., Yan, C. Grain Boundary Effects on Microstructural Stability of Nanocrystalline Metallic Materials**.** T. Tanski (Ed.), Study of Grain Boundary Character, InTechOpen (2017). **(ch. 7).**

2. Jonathan, R., Leslie H. J., John E. N., Michael F. T., Rodrigo, N., Shaofeng L., Tobin J. M., Antonio F. & Alberto S. Large modulation of carrier transport by grain-boundary molecular packing and microstructure in organic thin films. *nature. mater.* **8**, 952-958 (2009).

3. Zhiyang Y., Patrick R. C., Qin G., Denise Y., Yuanyao Z., Naixie Z., Gregory S. R., Michael W., Jian L., Martin P. H. Segregation-induced ordered superstructures at general grain boundaries in a nickel-bismuth alloy. *Science* **358**, 97–101 (2017).

4. Vleet, M. J. V., Weng, T., Li, X. & Schmidt, J. R. In Situ, Time-Resolved, and Mechanistic Studies of Metal−Organic Framework Nucleation and Growth. *Chem. Rev*. **118**, 3681-3721 (2018).

5. Aerts, A., Kirschhock, C. E. A., & Martens, J. A. Methods for in situ spectroscopic probing of the synthesis of a zeolite. *Chem. Soc. Rev.* **39**, 4626-4642 (2010).

6. Moor, P. E. A., Beelen, T. P. M., Komanschek, B. U., Beck, L. W., Wagner, P., Davis, M. E. & Van Santen, R. A. Imaging the Assembly Process of the Organic-Mediated Synthesis of a Zeolite. *Chem. Eur. J*. **5**, 2083-2088 (1999).

7. Davis, T.M. *et al.* Mechanistic principles of nanoparticle evolution to zeolite crystals. *Nature Mater.* **5**, 400-408 (2006).

8. Kirschhok, C. E. A., Ravishankar, R., Jacobs, P. A. & Martens, J. A. Aggregation Mechanism of Nanoslabs with Zeolite MFI-Type Structure. *J. Phys. Chem. B* **103**, 11021-11027 (1999).

9. De Yoreo, J. J. *et al.* Crystallization by particle attachment in synthetic, biogenic, and geologic environments. *Science* **349**, 6760 (2015).

10. Zheng, C., Greer, H. F., Chiang, C-Y. & Zhou, W. Microstructural study of the formation mechanism of metal–organic framework MOF-5. *CrystEngComm*. **16**, 1064-1070 (2014).

11. Patterson, J. P. *et al.* Observing the Growth of Metal−Organic Frameworks by in Situ Liquid Cell Transmission Electron Microscopy. *J. Am. Chem. Soc.* **137**, 7322-7328 (2015).

12. Zhou, H. C., Long, J. R., Yaghi, O. M. Introduction to Metal−Organic Frameworks. *Chem. Rev.* **112**, 673-674 (2012).

13. Furukawa, H., Cordova, K. E., O'Keeffe, M., Yaghi, O. M. The Chemistry and Applications of Metal-Organic Frameworks. *Science* **341**, 1230444 (2013).

14. Deng, H. *et al.* Large-Pore Apertures in a Series of Metal-Organic Frameworks. *Science* **336**, 1018-1023 (2012).

15. Li, P-Z. *et al.* Clicked Isoreticular Metal–Organic Frameworks and Their High Performance in the Selective Capture and Separation of Large Organic Molecules. *Angew. Chem*. **127**, 12939-12943 (2015).

16. Roy, X. & MacLachlan, M. J. Coordination Chemistry: New Routes to Mesostructured Materials. *Chem. Eur. J*. **15**, 6552-559 (2009).

17. Zhang, W. *et al.* Mesoporous Metal–Organic Frameworks with Size-, Shape-, and Space-Distribution-Controlled Pore Structure. *Adv. Mater*. **27**, 2923-2929 (2015).

18. Feng, L. *et al.* Creating Hierarchical Pores by Controlled Linker Thermolysis in Multivariate Metal−Organic Frameworks. *J. Am. Chem. Soc.* **140**, 2363-2372 (2018).

19. Jeong, S. *et al.* Topology Conversions of Non-Interpenetrated Metal−Organic Frameworks to Doubly Interpenetrated Metal−Organic Frameworks. *Chem. Mater*. **29**, 3899-3907 (2017).

20. *Materials Studio*, version 4.3; Accelrys: San Diego, CA, 2008.

21. Gao, C., Liu, S., Xie, L., Ren, Y., Cao, J. Sun, C. Design and construction of a microporous metal-organic framework based on the pillared-layer motif. *CrystEngComm*. **9**, 545−547 (2007).

Acknowledgement

I would like to express my deepest appreciation to my advisor Prof. Myoung Soo Lah for the continuous support and guidance during my degree course work. He always helped me to expend my knowledge and not to get out of right direction. I would also like to thank Prof. Hoi Ri Moon for her advice and feedback. Her varied perspectives have helped me to strengthen my work.

I want to thank to all lab members, Seung Bin Baek, Somi Won, Amitosh Sharma, Seungwan Han, Junmo Seong, Jaewoong Lim and Seonghwan Lee who have discussed researches. I also appreciate Minhak Oh, Sehyun Jeong, Sunyoung Shin, Jeongin Park, Dr. Dongwook Kim, Dr. Song xiaokai , Dr. Xinfang Liu, Dr. Dohyun Moon, Dr. Gyounghwa Jeong and other former members who gave suggestion about problems.

Finally, I am grateful to my family members and friends who have provided me through moral and emotional support in my life. Thanks for all your encouragement.